A scalable plant-resolving radiative transfer model based on optimized GPU ray tracing

B.N. Bailey[a], M. Overby[b], P. Willemsen[b], E.R. Pardyjak[a], W. F. Mahaffee[c], R. Stoll[a,*]

[a] *Department of Mechanical Engineering, University of Utah, Salt Lake City, UT, USA*
[b] *Department of Computer Science, University of Minnesota Duluth, Duluth, MN, USA*
[c] *U. S. Department of Agriculture - Agricultural Research Service, Horticulture Crops Research Laboratory, Corvallis, OR, USA*

Abstract

A new model for radiative transfer in participating media and its application to complex plant canopies is presented. The goal was to be able to efficiently solve complex canopy-scale radiative transfer problems while also representing sub-plant heterogeneity. In the model, individual leaf surfaces are not resolved, but rather vegetation is aggregated into isothermal volumes. Using the leaf angle distribution and leaf area density functions, the volumes realistically augment the radiation field through absorption and anisotropic scattering and re-emission. The volumes are grouped to form individual plants, and individual plants are grouped to form entire canopies. The model increases efficiency by performing ray tracing calculations on graphics processing units (GPUs) using the NVIDIA® OptiX™ and CUDA™ frameworks, and through efficient algorithms for radiation reflection, scattering, and emission. This efficiency allows for realistic representation of heterogeneity, while also allowing for the solution of problems with very large domains ($\sim 10^5$ trees) quickly on an inexpensive desktop workstation. Problem execution time scaled nearly linearly with the number of discrete elements in the domain. Model results are compared with experimental data collected from an array of radiation sensors within and above a grapevine canopy and an isolated tree. Agreement between simulated and measured values of shortwave and longwave radiation were very good, with model predictions generally within the expected measurement accuracy.

Keywords: Anisotropic radiation scattering, Graphics processing units, Participating media, ray tracing, Tree radiative transfer

*Corresponding author
Email address: rstoll@eng.utah.edu (R. Stoll)

Table 1: List of primary symbols used throughout the text

Symbol	Description	Units
a	leaf area density	m^{-1}
A	patch area	m^2
$E(r)$	ray energy at position r along its path	W
E_{ray}	initial ray energy ($r = 0$)	W
f_V	fraction of ray energy that does not undergo multiple scattering or absorption	-
g_L	leaf angle distribution function	-
$G(\theta')$	fraction of unit leaf area projected in the ray direction θ'	-
I	radiative intensity	W m^{-2} sr^{-1}
I_b	blackbody radiative intensity	W m^{-2} sr^{-1}
K	leaf specular reflectance reduction factor	-
n	index of refraction of leaf cuticle wax	-
N_k	number of rays launched from patch/volume k	-
$N(\theta', \psi')$	diffuse solar irradiance distribution function	-
r	ray path length through participating volume	m
$R_{L,\mathrm{diff}}$	absorbed incoming diffuse longwave radiative energy rate	W
$R_{L,\varepsilon}$	energy rate loss due to radiative emission	W
R_N	net radiation energy rate	W
R_{diff}	absorbed incoming diffuse radiative energy rate	W
R_{dir}	absorbed incoming direct radiative energy rate	W
$\boldsymbol{s}$	unit vector corresponding to the direction of reflection/scattering	-
$\boldsymbol{s'}$	unit vector corresponding to the direction of ray propagation	-
$\boldsymbol{s_L}$	unit vector corresponding to the leaf normal direction	-
$S_{NIR,\mathrm{dir}}$	incoming direct NIR flux directly above canopy height	W m^{-2}

$S_{PAR,\mathrm{dir}}$	incoming direct PAR flux directly above canopy height	W m^{-2}
$S_{L,\mathrm{diff}}$	incoming diffuse longwave flux directly above canopy height	W m^{-2}
$S_{NIR,\mathrm{diff}}$	incoming diffuse NIR flux directly above canopy height	W m^{-2}
$S_{PAR,\mathrm{diff}}$	incoming diffuse PAR flux directly above canopy height	W m^{-2}
T_L	leaf surface temperature	K
T_g	ground (patch) surface temperature	K
V	vegetation cell volume	m^3
$\alpha_{L,D}$	leaf tissue absorptivity	-
β	$= a\,G(\theta')$, attenuation coefficient	m^{-1}
ε_L	leaf emissivity	-
ε_g	patch (ground) emissivity	-
κ	absorption coefficient	m^{-1}
Ω	solid angle	sr
ψ	azimuthal angle of scattered/reflected direction ($\boldsymbol{s}$)	rad
ψ_s	solar azimuthal angle	rad
ψ'	azimuthal angle of ray propagation direction ($\boldsymbol{s'}$)	rad
Φ_D	diffuse scattering phase function	-
Φ_S	specular scattering phase function	-
ρ''	surface bidirectional reflectance distribution function	-
$\rho_{L,D}$	leaf tissue reflectivity	-
ρ_{Fr}	Fresnel reflectance	-
ρ_g	ground (patch) reflectivity	-
σ	$= 5.67 \times 10^{-8}$, Steffan-Boltzmann constant	W m^{-2} K^{-1}
σ_s	scattering coefficient	m^{-1}
$\tau_{L,D}$	leaf tissue transmissivity	-
θ	zenith angle of scattered/reflected direction ($\boldsymbol{s}$)	rad
θ_i	half the angle between $\boldsymbol{s'}$ and $\boldsymbol{s}$	rad

θ_L	leaf normal zenith angle	rad
θ_L^{sp}	leaf normal zenith angle corresponding to specular reflection from $\boldsymbol{s'}$ to $\boldsymbol{s}$	rad
θ_s	solar zenith angle	rad
θ_t	$= \sin^{-1}(\theta_i/n)$, Snell's law	rad
θ'	zenith angle of ray propagation direction ($\boldsymbol{s'}$)	rad
$\omega_{L,D}$	leaf single-scattering albedo for diffuse scattering	-
$\omega_{L,S}$	leaf single-scattering albedo for specular refelction	-
ω_L	leaf single-scattering albedo	-

1. Introduction

The transport of radiation through plant canopies is a physically complex phenomenon, which makes modeling this process difficult. Leaf and woody surfaces absorb, transmit, or scatter incoming irradiation, and also re-emit radiation themselves. On the whole, trees have evolved to live in groups or forests (Murray, 2011). These types of canopies can often be considered horizontally homogeneous, which reduces modeling difficulty (Ross, 1981). Primarily because of human intervention, plants have also been forced to adapt to a more isolated habitat. Humans have transformed natural forests through clear-cutting and management practices, and transported trees to urban areas that otherwise live in dense forests. This results in canopies with complicated geometries. The crowns of isolated vegetation are complex and three-dimensional, as they have adapted to maximize absorption of irradiation from all angles (Horn, 1971; Iwasa et al., 1985), making them difficult to model. Overall, understanding radiation interception and scattering in complex canopies is important for a wide range of urban and agricultural applications including urban microclimate (Dimoudi and Nikolopoulou, 2003), canopy growth (Russell et al., 1989; Hay and Porter, 2006), green infrastructure (Gill et al., 2007), plant water use and evapotranspiration (ET) (Nogués et al., 1998; Buckley et al., 2012), and remote sensing (Jones and Vaughan, 2010), among others.

Various strategies have been employed to model radiative transfer in complex environments such as a plant canopy, which may be grouped into two broad classes: deterministic and stochastic. Deterministic methods (e.g., Jeans, 1917; Chandrasekhar, 1950; Hottel and Cohen, 1958) involve directly obtaining an approximate numerical solution to the governing equation of radiative transfer in some form. These methods are generally preferred for problems with relatively simple geometries, as they are often computationally efficient and do not rely on statistical approximations. However, they can become inefficient and possibly unusable in the case of complex geometries or anisotropic reflection/scattering (Modest, 2013). Stochastic (Monte Carlo) ray tracing methods simulate the paths of individual 'bundles' of photons (Farmer and Howell, 1998). Their paths

are modified upon the occurrence of absorption, reflection, or scattering events, which are determined stochastically using mean free paths. These methods are able to handle geometries of arbitrary complexity, and therefore lend themselves to problems involving complex canopies. However, they also converge slowly as it takes a very large number of photon paths to reduce the variance in the sampled radiation field.

The above model classes have been adapted to predict the three-dimensional distribution of radiation in complex canopies. By necessity, these models must make compromises in terms of the level of physical description and computational cost. Models originally intended for use in homogeneous canopies have been shown to perform poorly when applied to complex, heterogeneous canopies (Asrar et al., 1992). Other models have been proposed that are able to resolve the general structure of individual trees (North, 1996; Cescatti, 1997; Stadt and Lieffers, 2000; Groot, 2004), or even heterogeneity within individual crowns (Kimes and Kirchner, 1982; Norman and Welles, 1983; Wang and Jarvis, 1990; Sinoquet et al., 2001). However, these classes of models have computational costs that scale poorly with increases in domain size, and are unlikely to be useful in problems involving urban forestry or kilometer-scale canopies with hundreds of thousands of trees. These models also struggle to include realistic radiation scattering because of its complexity, which has been demonstrated to be an important part of radiation transfer in canopies (Reyna and Badhwar, 1985; Ballaré et al., 1990; Kuusk, 1991). Even finer-scale models have been developed that resolve radiative interactions with individual leaves (Govaerts, 1995; Dauzat and Eroy, 1997; Soler et al., 2003; López-Lozano et al., 2011), which consequently increases computational demands even further. Many of the above models do not consider terrestrial radiation transport, as solar/visible radiation is the focus of their application (e.g., remote sensing, computer graphics). Simulating terrestrial radiation adds additional complexity, and is a critical component of the plant energy balance.

Computer graphics researchers focusing on visible light transport in complex environments have had to overcome similar challenges in managing physical complexity and computational cost. Graphics processing units (GPUs) on video cards were primarily developed for fast, concurrent matrix and vector operations associated with rasterization, simple direct illumination, and projection of geometry onto a 2D display. Current GPUs still support these basic computations, but the hardware design has been substantially modified to afford more complex computation by increasing the number of computing cores dedicated to parallel execution. These hardware changes have been driven initially by the demand for physical realism in video games, resulting in more advanced algorithms to simulate and approximate the transport of light (visible radiation). Consequently, this hardware can be found in nearly all personal computers and workstations. More recently, GPUs have been adapted for general purpose or GP-GPU computing to accelerate other types of computations (Owens et al., 2007).

This paper presents a ray tracing-based radiative transport model for use in complex canopies that is designed to exploit features of GPU architectures in

order to accelerate calculations. However, the method is applicable to radiative transport in any participating media, and can also be efficiently implemented on traditional CPU architectures. The model borrows methods commonly used in Monte Carlo ray tracing, and applies them in a deterministic manner to reduce the computational expense associated with the simulation of very large numbers of ray trajectories. The primary application of the framework is to drive other biophysical models that require accurate radiative fluxes at the leaf scale (e.g., plant growth, energy balance and leaf temperature, stomatal conductance). The use of accelerated computing methods along with the efficiency of the model algorithms allows for the simulation of canopy-scale problems on consumer-level computers, while also including the necessary detail and physical processes for accurate results.

This study is organized into three primary components. The first component details the model formulation, beginning with a brief model overview and transitioning into model specifics (§2). In the second component, a new field experiment is described, which was used to rigorously validate the model (§3). Finally, a computational study is presented to evaluate various model implementation strategies, and their implications on the ability to run very large, canopy-scale domain sizes (§4).

2. Model description

The radiative transfer model utilizes concepts from three separate methods traditionally used in the solution of radiative transfer problems with participating media: Monte Carlo ray tracing, the zonal method, and the discrete ordinates method (a summary of these methods can be found in standard radiation textbooks such as Howell et al., 2010; Modest, 2013). In the present method, a 'bundle' of photons with an initial energy value are sent either toward or away from a discrete surface area or volume of vegetation, and their path through the domain is tracked (we term this bundle path a 'ray'). In the event that the bundle passes through a volume of participating media (e.g., vegetation), the energy of the bundle is then augmented along its path through absorption, emission, and scattering according to the radiative transfer equation (RTE). The RTE can be written as (Modest, 2013)

$$\frac{\partial I(r;\boldsymbol{s}')}{\partial r} = -\kappa I(r;\boldsymbol{s}') - \sigma_s I(r;\boldsymbol{s}') + \kappa I_b(r) + \sigma_s \int_{4\pi} I(r;\boldsymbol{s}') \left(\frac{\Phi(r;\boldsymbol{s}',\boldsymbol{s})}{4\pi} \right) d\Omega, \quad (1)$$

where $I(r,\boldsymbol{s}')$ is the radiative intensity at position r along the direction of propagation $\boldsymbol{s}'$, κ and σ_s are the absorption and scattering coefficients, respectively, $I_b(r)$ is the blackbody intensity at position r, $\Phi(r;\boldsymbol{s}',\boldsymbol{s})$ is the scattering phase function at position r for incident direction $\boldsymbol{s}'$ and scattered direction $\boldsymbol{s}$, and $d\Omega$ is a differential solid angle. We also define $\beta = \kappa + \sigma_s$ as the attenuation coefficient. The propagation and scattered directions are represented by their spherical coordinate angles (θ', ψ') and (θ, ψ) (zenith, azimuth).

Moving left to right in Eq. 1, term I is the rate of change of intensity with position along the ray path, term II is intensity reduction by absorption, term III is intensity reduction by out-scattering, term IV is the addition of intensity through emission by neighboring surfaces and participating media, and term V is the addition of intensity through in-scattering.

In the present model, each of the terms in Eq. 1 are evaluated using simulated ray path traces. Rays are launched from surfaces and volumes of participating media with some initial energy content. The energy that is lost by the ray due to participating media is calculated by evaluating Eq. 1 along the ray's path with no source (positive) terms. Some of this lost energy is due to scattering away from the direction of propagation, which is tracked through additional ray traces. Radiation absorbed by surfaces and volumes of participating media due to all rays is summed (less radiative losses) to obtain the net radiation.

When dealing with atmospheric applications combined with vegetation, it is convenient to use a three-band approximation that separates the spectrum into two 'shortwave' bands, which correspond to all radiation emitted by the sun, and a 'longwave' band, which corresponds to all radiation emitted by terrestrial matter (e.g., soil, trees, vapors). The shortwave band is separated into photosynthetically active radiation (PAR) and near-infrared radiation (NIR) bands. This is because plant leaves have markedly different radiative properties in these two bands (Jones and Vaughan, 2010). Leaves are extremely efficient at absorbing solar irradiation in the PAR band, and are much less efficient absorbers in the NIR band. The present model is not restricted to these band definitions, as the radiation spectrum could be divided into an arbitrary number of bands. For practical purposes, we define the PAR band as any solar irradiation with wavelength less than 660 nm, and NIR as the rest of the solar spectrum.

Given this three-band approximation, the net radiation balance on a surface or volume can be expressed as

$$R_N = R_{PAR,\text{dir}} + R_{NIR,\text{dir}} + R_{PAR,\text{diff}} + R_{NIR,\text{diff}} + R_{L,\text{diff}} - R_{L,\varepsilon}, \qquad (2)$$

where R_N is net energy rate in Watts due to radiative heat transfer, which is balanced by (denoting incoming energy as positive) $R_{PAR,\text{dir}} + R_{NIR,\text{dir}}$ the net absorbed direct solar radiative energy rate, $R_{PAR,\text{diff}} + R_{NIR,\text{diff}}$ the net absorbed diffuse solar radiative energy rate, $R_{L,\text{diff}}$ the net absorbed diffuse longwave radiative energy rate, and $-R_{L,\varepsilon}$ the energy rate loss due to radiative emission. The average radiative heat flux can be calculated by dividing R_N by the (two-sided) leaf area within the volume ($2aV$).

The remainder of this section is devoted to outlining the procedure for calculating each of the terms in Eq. 2 in more detail. Section 2.1 describes how the domain is discretized. Procedures for the launching of rays and assigning their associated energy are detailed in Sect. 2.2. The augmentation of ray energy in the event of surface or volume intersections is described in Sect. 2.3.

2.1. Domain discretization

In the case of a vegetative canopy, the domain consists of a number of types of solid surfaces that can absorb, scatter, and emit radiation. In this model, individual leaf surfaces within the crown are not resolved, but rather aggregated into discrete isothermal cells with homogeneous properties. Thus, each cell can be treated as a homogeneous volume of participating media analogous to the zonal method for radiative transfer (Hottel and Cohen, 1958; Hottel and Sarofim, 1967). Note that the air within the cell is assumed to be transparent to all wavelengths of radiation.

The amount of leaves within the volumes is represented by the leaf area density, which is the one-sided leaf surface area per unit volume. The effects of the orientation of individual leaves are represented by a probability density function for leaf elevation angle g_L, which is used to calculate directionally-dependent scattering, absorption, and attenuation coefficients as well as a scattering phase function that is dependent on incoming and scattered ray directions. Woody surfaces are neglected, as it is assumed that their contribution is small compared to leaves (Ross, 1981).

The shape of the volumes is arbitrary, although they should be sufficiently small that physical properties (leaf area density, leaf temperature, etc.) may be considered constant within the volume, and large enough that they are much bigger than the size of an individual leaf. Analogously, the ground surface is discretized into isothermal sub-areas with constant properties that will hereafter be referred to as 'patches'. Surface roughness is accounted for by assigning an appropriate bidirectional reflectance distribution function BRDF. Unlike other models (e.g., Kimes and Kirchner, 1982), space within the domain that contains no leaves is not discretized, which substantially reduces memory requirements and efficiency. Ray paths that intersect the upper boundary are terminated, and rays that intersect the lower boundary (ground) are absorbed/reflected as described below. Ground and vegetation beyond the horizontal boundaries are neglected and it is assumed that the domain size is large enough that edge effects are negligible. A schematic of a sample domain discretization is shown in Fig. 1.

2.2. Launching of rays

Longwave Emission by Patches and Volumes: To calculate longwave energy exchange due to emission of radiation by patches and participating volumes, rays were sent outward from all patches and volumes. Rays are sent in a hemispherical pattern from the center of patches (Fig. 2a), with directions chosen to uniformly fill the hemisphere using the 'spiral points' method of Saff and Kuijlaars (1997). Similarly, rays are sent from the outside surface of volumes in a spherical pattern (Fig. 2b).

The energy of a single ray emanating from a particular ground patch can be expressed as

$$E_{\text{ray}} = 2\varepsilon_g \sigma T_g^4 A \cos\theta' / N_k, \tag{3}$$

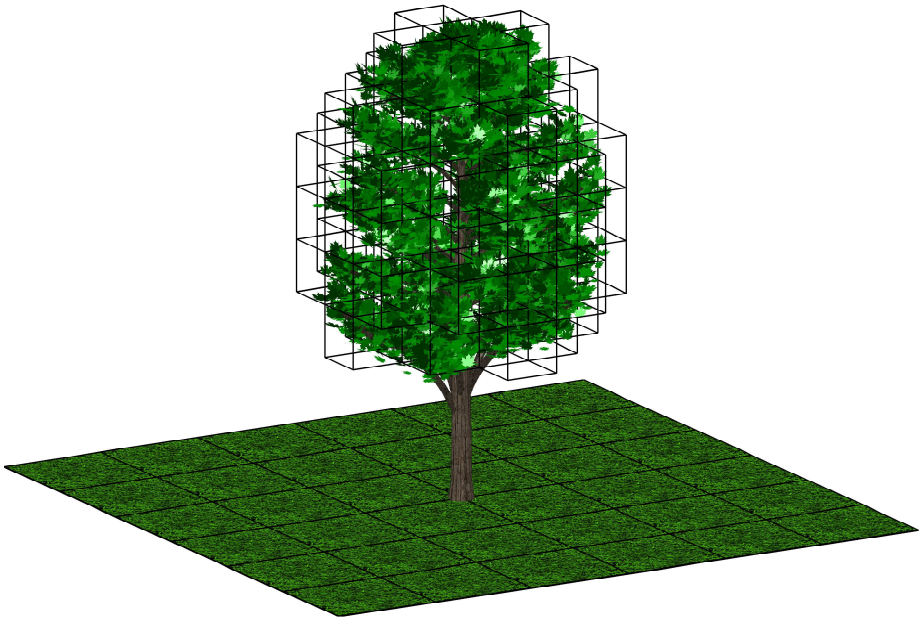

Figure 1: Sample discretization that may be used to represent a single tree crown. The ground surface is discretized into uniform rectangular elements. The tree crown is discretized into uniform rectangular prism elements.

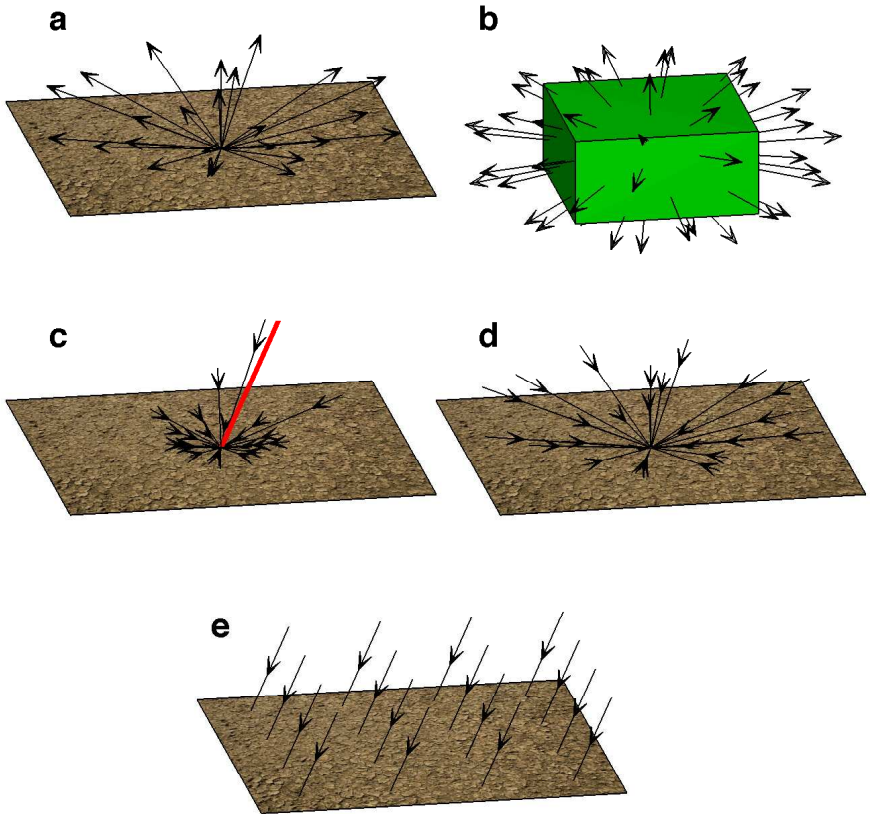

Figure 2: Schematic depicting the five types of ray launches to calculate (a) patch emission, (b) volume emission, (c) incoming shortwave diffuse, (d) incoming longwave diffuse, (e) incoming shortwave direct. Ray lengths indicate relative energy content.

where ε_g is the ground total emissivity, $\sigma = 5.67 \times 10^{-8}$ W m^{-2} K^{-1} is the Stefan-Boltzmann constant, T_g is the ground temperature [K], A is the patch area [m^2], θ is the zenith angle of the ray direction [rad], and N_k is the number of rays launched from the patch. Since the integral of $\cos\theta'$ over the hemisphere is equal to 0.5, the factor of 2 is needed to ensure that the total energy leaving the patch is $\varepsilon_g \sigma T_g^4 A$.

The energy of a ray emanating from a volume is (Hottel and Cohen, 1958)

$$E_{\text{ray}} = 4\kappa(\theta')\varepsilon_L \sigma T_L^4 V \, f_V(\theta')/N_k, \tag{4}$$

where ε_L is the leaf total emissivity, T_L is the leaf surface temperature, and V is the cell volume.

The factor f_V is the fraction of radiation that actually leaves the volume after absorption and scattering within the volume for emission in the direction of θ'. The procedure for calculating f_V is given in § 2.4.

In this paper, it is assumed that T_g and T_L are known throughout the domain. A model to calculate these temperatures through energy balances will be presented in a future publication.

Diffuse Irradiation: Incoming diffuse irradiation (shortwave and longwave) from the sky is calculated by sending a hemispherical pattern of rays toward the center of patches only (Fig. 2c,d). Ray directions were chosen in the same way as described above for longwave emission, except with their direction of travel reversed. Rays are traced from the edge of the computational domain back to the center of the patch from which they originated.

The total longwave diffuse energy for all rays originating from a patch (which is the energy hitting an unobstructed patch) is $S_{L,\text{diff}} A$, where $S_{L,\text{diff}}$ is the incoming diffuse longwave sky irradiation flux above the canopy. The energy of an individual ray is

$$E_{\text{ray}} = 2\, S_{L,\text{diff}} A \cos\theta' / N_k. \tag{5}$$

Shortwave diffuse irradiation is highly dependent on direction (θ', ψ'), and usually decreases rapidly away from the sun direction (Monteith and Unsworth, 2008). The angular solar radiance distribution $N(\theta', \psi')$ was calculated using the model of Harrison and Coombes (1988). $N(\theta, \psi)$ was normalized such that a sum over the hemisphere yielded a value of 1.0. The ray energy for diffuse solar radiation is then

$$E_{\text{ray}} = 2\, S_{PAR,\text{diff}}\, N(\theta', \psi')\, A \cos\theta', \tag{6a}$$

$$E_{\text{ray}} = 2\, S_{NIR,\text{diff}}\, N(\theta', \psi')\, A \cos\theta', \tag{6b}$$

where $S_{PAR,\text{diff}}$ and $S_{NIR,\text{diff}}$ are the flux of incoming diffuse PAR and NIR irradiation above the canopy, respectively.

Direct Solar Irradiation: Shortwave energy exchange was calculated by sending a series of collimated rays toward patches in the direction of the sun (θ_s, ψ_s). The rays were launched such that they intersected a given patch in

a two-dimensional gridded pattern (Fig. 2e). An individual ray was assigned a value of

$$E_{\text{ray}} = S_{PAR,\text{dir}} A / N_k, \tag{7a}$$
$$E_{\text{ray}} = S_{NIR,\text{dir}} A / N_k, \tag{7b}$$

where $S_{PAR,\text{dir}} + S_{NIR,\text{dir}}$ is the shortwave radiative flux just above the highest tree-top.

2.3. Ray scattering and absorption

In the context of ray tracing, absorption and scattering of radiation in complex participating media is commonly calculated using a Monte Carlo (stochastic) approach (North, 1996; Farmer and Howell, 1998). The frequency of each absorption or scattering event is calculated as a function of a randomly generated number and the absorption or scattering coefficient. A scattering event causes the ray's direction to change, where this direction is chosen using the scattering phase function and another random number. The absorption of radiation is handled in a similar manner, except that when an absorption event occurs the ray's path is terminated. The drawback of this stochastic approach is that a very large number of rays are required for the method to converge, which can be computationally inhibiting (Farmer and Howell, 1998).

We instead use a different approach to compute absorption and scattering similar to that of Kimes and Kirchner (1982) that substantially reduces the number of rays required for the calculations to converge. This approach also removes the stochastic element, as it is completely deterministic. Instead of terminating the ray's trajectory upon an absorption event, the ray's energy is simply reduced by some fraction. If a ray is reflected by a patch or scattered by a volume, this energy is continually accumulated until all ray traces have ceased. The reflected/scattered energy is traced by launching a new set of rays in a hemispherical (from patches) or spherical (from volumes) pattern. This process continues recursively until the energy of all rays drops below some arbitrarily small threshold. To ensure 100% energy conservation, this very small amount of remaining energy is deposited in the most recently intersected patch or volume.

2.3.1. Leaf optical model

Photon-leaf intersections are modeled by a combination of specular reflection due to leaf epicuticular wax and diffuse scattering by leaf tissue, as illustrated by Fig. 3.

Specular Reflection: Upon ray intersection with a leaf, some fraction of its energy $\rho_{L,S}$ is first specularly reflected by leaf epicuticular wax. This fraction is the specular single-scattering albedo and is calculated as the product of the Fresnel reflectance and a correction factor

$$\omega_{L,S} = K \, \rho_{Fr}, \tag{8}$$

where the Fresnel reflectance ρ_{Fr} is calculated as the average over polarization states

$$\rho_{Fr} = \frac{1}{2}\left[\frac{\sin^2(\theta_i+\theta_t)}{\sin^2(\theta_i-\theta_t)} + \frac{\tan^2(\theta_i+\theta_t)}{\tan^2(\theta_i-\theta_t)}\right], \tag{9}$$

θ_i is half the angle between $\boldsymbol{s}'$ and $\boldsymbol{s}$, $\theta_t = \sin^{-1}(\sin\theta_i/n)$ (Snell's law), and n is the index of refraction of the leaf wax. The factor K accounts for the fact that a leaf is not a perfectly plane reflector as assumed by Fresnel's equation. For a plane, continuous canopy as viewed from above, $0 < K < 1$ in general because the canopy top is far from a flat, plane reflector (Ghosh et al., 1993). However, measurements of individual leaf surfaces indicate that K can be (and usually is) greater than 1, and that K differs significantly between and adaxial and abaxial sides of the leaf (Brakke, 1994). We used a linear fit to the data of Brakke (1994) for summertime *Acer rubrum* to estimate K (measurements are given for only two view angles θ_i, thus necessitating a linear fit)

$$K_{ad} = 1.25\,\theta_i + 0.9, \tag{10a}$$

$$K_{ab} = 0.31\,\theta_i + 1.0, \tag{10b}$$

where subscripts *ad* and *ab* refer to coefficients for the adaxial and abaxial leaf sides, respectively. A ray is assumed to interact with the adaxial side of the leaf when the leaf angle for specular reflection θ_L^{sp} (see Eq. B.5) is less than $\pi/2$. Similarly, the ray interacts with the abaxial side when $\theta_L^{sp} \geq \pi/2$.

Diffuse scattering: The remaining fraction of energy that is not specularly reflected by the air-wax interface (i.e., $1-\omega_{L,S}$) is assumed to enter the leaf tissue. Further scattering occurs due to the many differences in refraction index throughout the leaf. It is assumed that collectively the leaf tissue scatters energy according to a bi-Lambertian distribution (Ross, 1981). The fraction of initial ray energy scattered by the leaf tissue is $(1-\omega_{L,S})\,\omega_{L,D}$, where $\omega_{L,D}$ is the diffuse single-scattering albedo which is the sum of the leaf reflectivity ($\rho_{L,D}$) and transmissivity ($\tau_{L,D}$), respectively. We note that $\rho_{L,D}$ and $\tau_{L,D}$ have a strong dependence on wavelength, which is accounted for by assigning appropriate values for the PAR, NIR, and longwave portions of the spectrum. The remaining energy that was not scattered is absorbed by the leaf, which is $(1-\omega_{S,D})\,(1-\omega_{L,D})$.

Total scattering: The total fraction of initial energy that is scattered by the leaf is the leaf single-scattering albedo

$$\omega_L = \omega_{L,S} + (1-\omega_{L,S})\,\omega_{L,D}. \tag{11}$$

The fraction of initial energy that is absorbed by the leaf is then $1-\omega_L$.

2.3.2. Volume intersections

As previously mentioned, the attenuation of radiation by discrete volumes of leaves is not modeled by accounting for the effects of individual leaves. Instead,

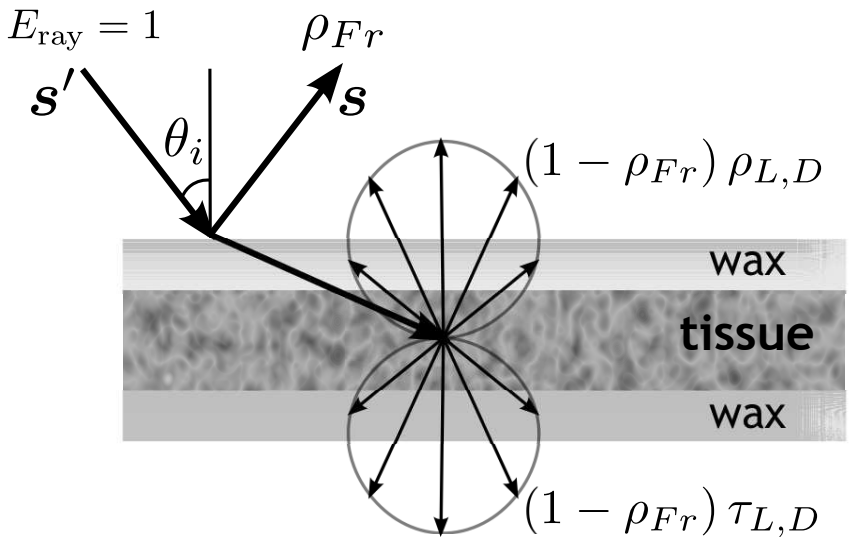

Figure 3: Leaf optical model used to calculate the scattering phase function. Example is given for an initial ray strength of unity.

it is modeled by assuming the leaves can be represented statistically. Therefore, the leaf optical model (§2.3.1) must be aggregated over a volume of leaves in order to calculate an appropriate attenuation coefficient and scattering phase function.

An equation describing the attenuation of a ray through a homogeneous participating media can be found by removing all incoming (positive) terms on the r.h.s. of Eq. 1 and replacing intensity with the energy rate value associated with the given ray. The solution of the resulting equation gives the well-known Beer-Lambert law

$$\frac{E(r+\Delta r)}{E(r)} = \exp\left(-\beta\,\Delta r\right), \tag{12}$$

where $E(r)$ is the ray energy entering the volume, $E(r+\Delta r)$ is the ray energy at volume exit, and Δr is the path length of the ray through the volume. For a volume of leaves, the attenuation coefficient $\beta = a\,G(\theta')$, where a is the one-sided leaf area density (LAD) of the volume, and $G(\theta')$ is the Ross-Nilson G-function, which is the fraction of a unit area of foliage projected in the direction of θ' (Ross, 1981).

As the ray leaves the volume, the ray simply continues on its path with some fraction of the energy that it had when it entered the volume (i.e., $\exp(-\beta\Delta r)$). The fraction of energy that was not transmitted through the volume ($1 - \exp(-\beta\Delta r)$) is partitioned into either absorbed or scattered energy. The absorbed fraction $(1-\omega_L)$ is accumulated in an energy buffer for that particular volume. The scattered fraction is then partitioned into three additional components: energy that is scattered and leaves the volume with no interaction (single scattering), energy that is scattered and absorbed by other leaves before leaving the volume, and energy that is scattered and then scattered again before leaving the volume (multiple scattering). The energy partitioning process is detailed in Fig. 4.

At this point, we are left with some amount of scattered energy that must be traced as it leaves the volume (i.e., sum of single and multiply scattered energy E_{scatt}). This is done by launching rays in a spherical pattern away from the volume. The scattered energy is divided amongst rays according to

$$E_{\text{ray}} = E_{\text{scatt}}\left[\omega_{L,S}\frac{\Phi_S}{4\pi} + (1-\omega_{L,S})\,\omega_{L,D}\frac{\Phi_D}{4\pi}\right], \tag{13}$$

where E_{scatt} is the total amount of scattered energy that leaves the volume, and Φ_S and Φ_D are the scattering phase functions due to specular and diffuse reflection, respectively. The scattering phase functions are dependent on the leaf angle distribution function and the leaf single-scattering albedos (see Appendix A).

This new set of rays launched from the volume will then intersect other patches/volumes, leaving some amount of energy to again be scattered. Thus the scattering continues iteratively until the amount of energy to be scattered becomes arbitrarily small.

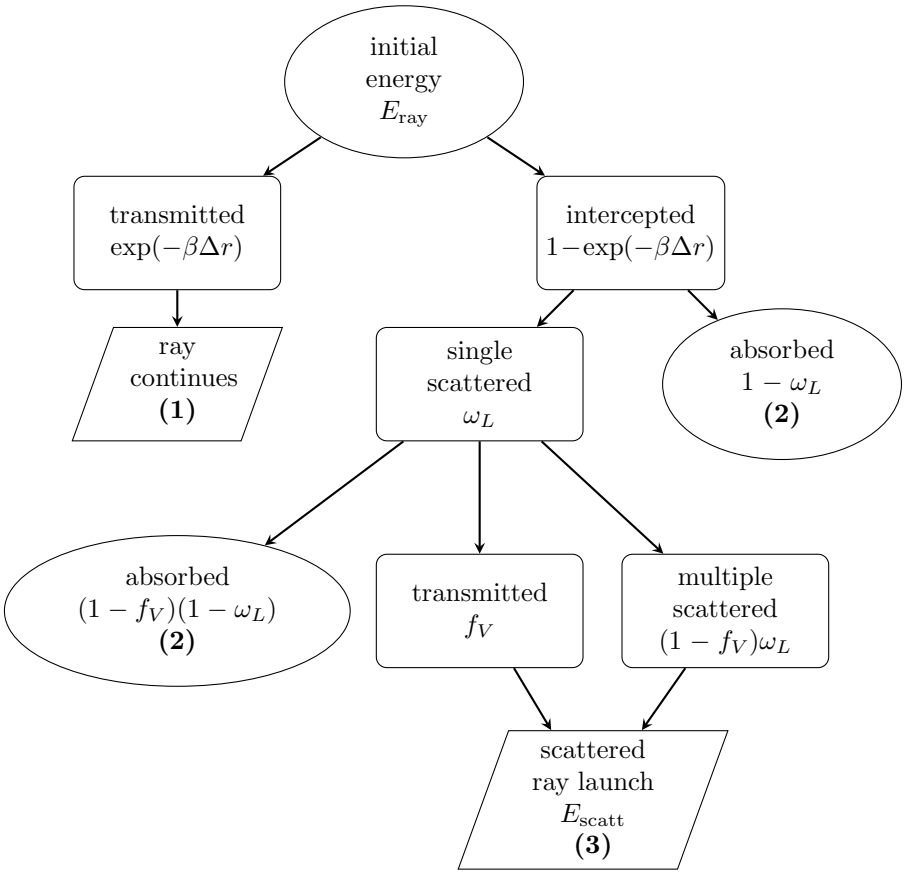

Figure 4: Partitioning of ray energy upon intersection with a vegetation volume. The ray's initial energy (E_{ray}) is partitioned into three outcomes: (1) the ray continues along its path with some fraction of its initial energy content, (2) some fraction of the ray's initial energy is absorbed by the volume, and (3) some fraction of the ray's initial energy is scattered away from the volume which is tracked through a new ray launch (E_{scatt}).

2.3.3. Patch intersections

Energy absorption and reflection by patches is similar to that of volumes, except that energy is absorbed according to the patch absorptivity and the remaining energy is reflected into the hemisphere above instead of a sphere. As a ray intersects a patch with energy $E(r)$, the patch absorbs energy of $\alpha_g E(r)$, where α_g is the ground absorptivity which is different for the PAR, NIR, and longwave bands. The remaining energy is reflected back into the hemisphere above. In the case of isotropic (diffuse) reflection, a hemisphere of rays are launched from the center of the patch each with energy of $2\rho_g E(r)\cos\theta\,/N_k$. For anisotropic reflection, a hemisphere of rays are launched from the center of the patch each with a directionally-dependent energy based on the surface bidirectional reflectance distribution function (BRDF) $\rho''(\boldsymbol{s'}, \boldsymbol{s})$. The energy given to an outgoing (reflected) ray is $2E(r)\rho''(\boldsymbol{s'}, \boldsymbol{s})\cos\theta/N_k$, where to total amount of energy leaving the patch is $(1-\alpha_g)E(r)$. The BRDF was calculated according to the model of Roujean et al. (1992), which requires three input parameters: k_0, k_1, k_2. Rather than directly integrating the BRDF to get the ground reflectivity, we used the polynomial approximation of the integral given by Roujean et al. (1992) (requires the same three input parameters). Like volume scattering, patch reflection also proceeds iteratively until the amount of energy to be reflected becomes arbitrarily small. These patch iterations are not performed separately from the volume scattering iterations, but rather concurrently since the two are linked.

2.4. Calculation of f_V

The factor f_V is the fraction of energy that is emitted or scattered by leaves within a volume that makes it to the edge of the volume without being again absorbed or scattered by other leaves within the same volume. f_V was calculated similar to (Hottel and Cohen, 1958), except that we used a ray tracing procedure to evaluate the integral. Rays were sent at a given direction θ' from a uniform grid of points within the volume with an initial energy of 1.0. This energy is then attenuated using Eq. 12 until the ray exits the volume. f_V is the average energy value of all rays sent in the direction θ' as they leave the volume. For relatively small volumes, f_V should be close to 1, as there is a higher probability that radiation emitted/scattered by leaves will leave the volume without being absorbed or scattered by other leaves within the same volume. As the volume size is increased, f_V decreases toward 0. Therefore, this factor is important in removing the grid-dependence of scattering and emission.

This factor is quite expensive to calculate, and should not be done for each emission event. If memory is available, this factor can be pre-computed once for every volume and re-used many times. If memory is not available, f_V can be approximated by launching one set of rays in a hemisphere from the center of the volume similar to Kimes and Kirchner (1982). This gives a reasonable approximation, but results in slightly lower f_V values.

3. Field experiment and model validation

Two experimental campaigns were performed during the Summer of 2013 to collect relevant data for validation of the radiation model. The first (VINEYARD) was conducted in a grapevine canopy (*Vitis vinifera*) in Oregon, USA (44° 49′ 28″ N 123° 14′ 17″ W) between 9 August and 24 August, 2013. This type of canopy was chosen because it is perhaps one of the simplest heterogeneous canopy geometries, as the canopy is quasi-homogeneous along the row direction and has regular intervals of heterogeneity in the row-normal direction. The canopy was oriented such that the rows ran almost exactly North-South. The rows were approximately 0.5 m wide and were spaced at 2.5 m. Vegetation was present at heights between 0.7 and 2.2 m. Further details about the experimental site can be found in Miller et al. (2014).

To explore model performance in the case of isolated vegetation, an experiment was conducted (ISOTREE) on a relatively isolated Freeman maple (*Acer x Freemanii*) on the University of Utah campus (40° 46′ 0″ N 111° 50′ 45″ W) between 1 July and 31 July, 2013. The tree was surrounded by a grassy area, with the nearest trees and buildings about 20 and 35 meters away, respectively. This meant that the entire tree crown was in direct sunlight from approximately 0900 to 1800 local time. The tree crown was approximately ellipsoidal which was centered at a height of approximately 4 m, with a horizontal radius of 2 m and a vertical radius of 3.25 m.

In general, validation of three-dimensional canopy radiation models is relatively weak, owing to the fact that it is difficult to measure the three-dimensional radiation field at multiple wavelengths within complex canopies. The most common procedure for validating these types of models is to place one or more quantum (PAR) sensors at various locations such that it is shaded by vegetation (e.g., Wang and Jarvis, 1990; Sinoquet et al., 2001; Groot, 2004). The ratio of the shaded sensor value to the above-canopy value is then compared for measured values and model predictions. However, this is not a good test of radiation scattering (which is neglected by nearly all previous 3D models), as leaves are efficient absorbers in the PAR band. In the NIR band, scattering is sure to be much more important as leaves are poor absorbers in this band. As a result, we have chosen to not only validate using PAR attenuation, but also by using additional sensors that focus on scattered radiation. This was accomplished by placing a downward-facing shortwave sensor (305-2800 nm) above vegetation to measure reflected and scattered radiation. Since the sensor was placed above vegetation, most of the radiation that was measured was due to scattering by leaves rather than reflection from the ground, thus making it a strong validation test.

To evaluate the terrestrial radiation model, a downward-facing longwave sensor (5,000-50,000 nm) was placed above vegetation. The downward-facing longwave sensor is a strong test of the longwave emission model, since most upward longwave radiation is due to emission (both the ground and leaf surfaces have low reflectivities in the longwave band).

Table 2: Model inputs for VINEYARD and ISOTREE validation test cases.

variable	VINEYARD value	ISOTREE value	source
a	2.0-6.5 m^{-1}	0.8-1.7 m^{-1}	measured
g_L	0.08-2.8	0.0-5.2	measured
$\rho_{L,D}$ (PAR)	0.056	0.050	Hosgood et al. (2005)
$\tau_{L,D}$ (PAR)	0.042	0.079	Hosgood et al. (2005)
$\rho_{L,D}$ (NIR)	0.425	0.348	Hosgood et al. (2005)
$\tau_{L,D}$ (NIR)	0.334	0.465	Hosgood et al. (2005)
$\rho_{L,D}$ (LW)	0.015	0.015	Kirchoff's Law
$\tau_{L,D}$ (LW)	0.015	0.015	Kirchoff's Law
ε_L	0.97	0.97	Campbell and Norman (1998)
ε_g	0.97	0.97	Campbell and Norman (1998)
n_{PAR}, n_{NIR}	1.5	1.5	Vanderbilt and Grant (1985)
n_{LW}	1.1	1.1	Allen et al. (1969) (estimated)
$\{k_0, k_1, k_2\}$ (PAR)	$\{0.278, 0.063, 0.553\}$	$\{0.146, 0.037, 0.372\}$	Roujean et al. (1992)
$\{k_0, k_1, k_2\}$ (NIR)	$\{0.342, 0.074, 0.666\}$	$\{0.326, 0.043, 0.656\}$	Roujean et al. (1992)
ρ_g	0.03 $(=1-\varepsilon_g)$	0.03 $(=1-\varepsilon_g)$	Kirchoff's Law

3.1. Model inputs

For many physical models, adding complexity is usually accompanied by the addition of new model parameters that can often be difficult to specify. As discussed by Passioura (1973), this leads to the temptation to 'tweak' or 'tune' these parameters until satisfactory results are obtained. Our goal for this validation study is to reduce *ad hoc* tuning of model inputs as much as possible in an attempt to test the model physics and not our ability to tune coefficients. This was done be either directly measuring model parameters, or using data sets reported in the literature.

Required model inputs for the validation cases are listed in Table 2. A discussion of these inputs is given below.

3.1.1. Leaf and ground optical properties

Optical properties for leaves were estimated using values reported in the literature. Leaf reflectivity and transmissivity for shortwave radiation were calculated using the LOPEX93 data set (Hosgood et al., 2005). The measured reflectivity and transmissivity spectra were integrated assuming the shortwave spectrum follows the solar energy distribution of Henderson (1977). For VINEYARD, spectra were available for *V. vinifera* (LOPEX sample #106). No spectra

were available from the LOPEX data for Freeman maple. For IsoTree, we used the spectra for *Acer pseudoplatanus* (sycamore maple) as a substitute (LOPEX sample #52). A summary of calculated shortwave leaf reflectivities and transmissivities can be found in Table 2.

In the longwave regime, leaves are close to blackbodies with emissivities near unity (Monteith and Unsworth, 2008; Jones and Vaughan, 2010). Therefore we assumed a leaf emissivity of 0.97. According to Kirchoff's Law, this means that $\rho_{L,D} + \tau_{L,D} = 0.03$. We assumed that $\rho_{L,D} = \tau_{L,D} = 0.015$. It is noted that longwave radiation can also be specularly reflected by leaves if $n > 1$ in this spectral band.

We assumed a constant value for the leaf wax index of refraction of $n = 1.5$ for the PAR and NIR bands (Vanderbilt and Grant, 1985; Nilson and Kuusk, 1989; Brakke, 1994). In the longwave band, it is likely that n is significantly smaller. We estimated a value of $n = 1.1$ based on data reported by Allen et al. (1969).

The Roujean et al. (1992) coefficients must be specified for each ground patch. For Vineyard, the ground consisted of roughly 1/3 annual grass and 2/3 plowed dirt. Therefore, we used a weighted average of the coefficients given by Roujean et al. (1992) for annual grass and plowed field, which gave $\{k_0, k_1, k_2\} = \{0.2781, 0.0633, 0.5531\}$ for the PAR band, and $\{k_0, k_1, k_2\} = \{0.3423, 0.0743, 0.6657\}$ for the NIR band. Fitted coefficients were not available for the longwave band, and therefore we assumed that the soil was a Lambertian reflector with a reflectivity equaling $\rho_g = 1 - \epsilon_g = 0.03$ (Kirchoff's Law). For Isotree, it was assumed that the ground was similar to the 'grass lawn' examined by Kimes (1983). However, the grass below Isotree was very dry for an urban lawn. Therefore, we used an average of the Roujean et al. (1992) coefficients for 'grass lawn' and 'plowed field', which is $\{k_0, k_1, k_2\} = \{0.1455, 0.0365, 0.372\}$ for the PAR band, and $\{k_0, k_1, k_2\} = \{0.3255, 0.0425, 0.656\}$ for the NIR band. The longwave reflectivity of the grass was also specified according to Kirchoff's Law.

3.1.2. Biophysical model parameters

The vertical distribution of LAD for Vineyard was measured directly using destructive methods. Measurements of LAD were performed by harvesting a representative number of leaves and determining leaf area through planimetric methods (Jonckheere et al., 2004). Area density was then calculated by dividing by the total volume from which the leaves were harvested. The LAD was assumed to change only with vertical height and not with horizontal position within a row (Fig. 5a).

The LAD distribution for IsoTree was estimated using an LAI2000 Plant Canopy Analyzer system (LI-COR, Lincoln, NE USA) (Fig. 5b). Three independent measurements were made just below the crown facing each of the four cardinal directions using the 90° lens cap as described in the user's manual. A continuous 'egg' function was fit to the four data points, which was used to

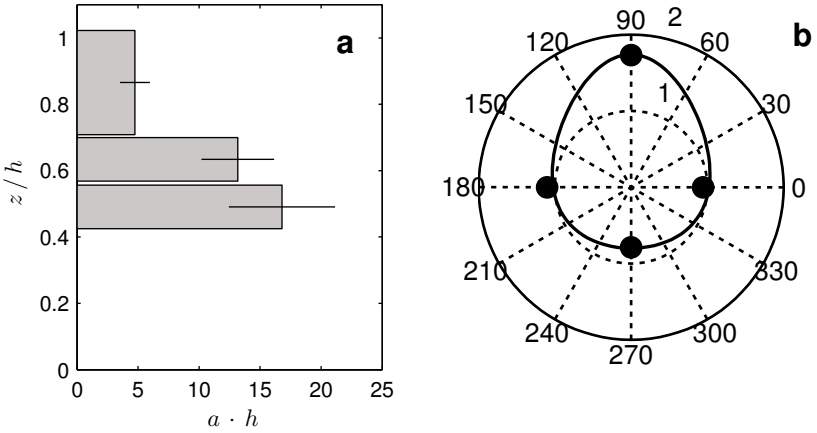

Figure 5: Measured leaf area density distributions. (a) shows the vertical profile of LAD for VINEYARD (LAD is assumed constant in the horizontal) normalized by the row height. Error bars denote ±1 standard deviation for measurements of individual vines. (b) gives measured LAD values (ISOTREE) for the four cardinal directions (0°=North, 90°=West, etc.), denoted by filled circles, and a continuous function fitted to the measurements, denoted by a solid line (LAD is assumed constant in the vertical).

specify the LAD of each vegetation volume

$$x = 1.1\frac{\cos\psi}{1+0.2y}, \tag{14a}$$

$$y = 0.47 + 1.27\sin\psi, \tag{14b}$$

$$a(\psi) = \left(x^2 + y^2\right)^{1/2}, \tag{14c}$$

where ψ is the azimuth angle of the vegetation volume relative to the trunk ($\psi = 0$ is North and increases counter-clockwise). The vertical distribution of LAD was assumed to be constant.

The distribution of leaf inclination was measured for both VINEYARD and ISOTREE using a digital protractor. For VINEYARD 80 measurements were performed (Fig. A.12a), and 120 measurements were performed for ISOTREE (Fig. A.12b). These measurements were used to calculate $G(\theta')$ through direct integration (detailed in Appendix A), and also the scattering phase function using a method adapted from Ross (1981) and Vanderbilt and Grant (1985) (detailed in Appendix B).

3.2. Model forcing measurements

Measured values used to drive the validation simulations were sampled at 1 Hz and averaged over 15 minute periods for two complete diurnal cycles with clear sky conditions. Since clear-sky radiation measurements show negligible diurnal variation, two days were deemed sufficient for comparison. Values are shown in Fig. 6, each of which are described separately below.

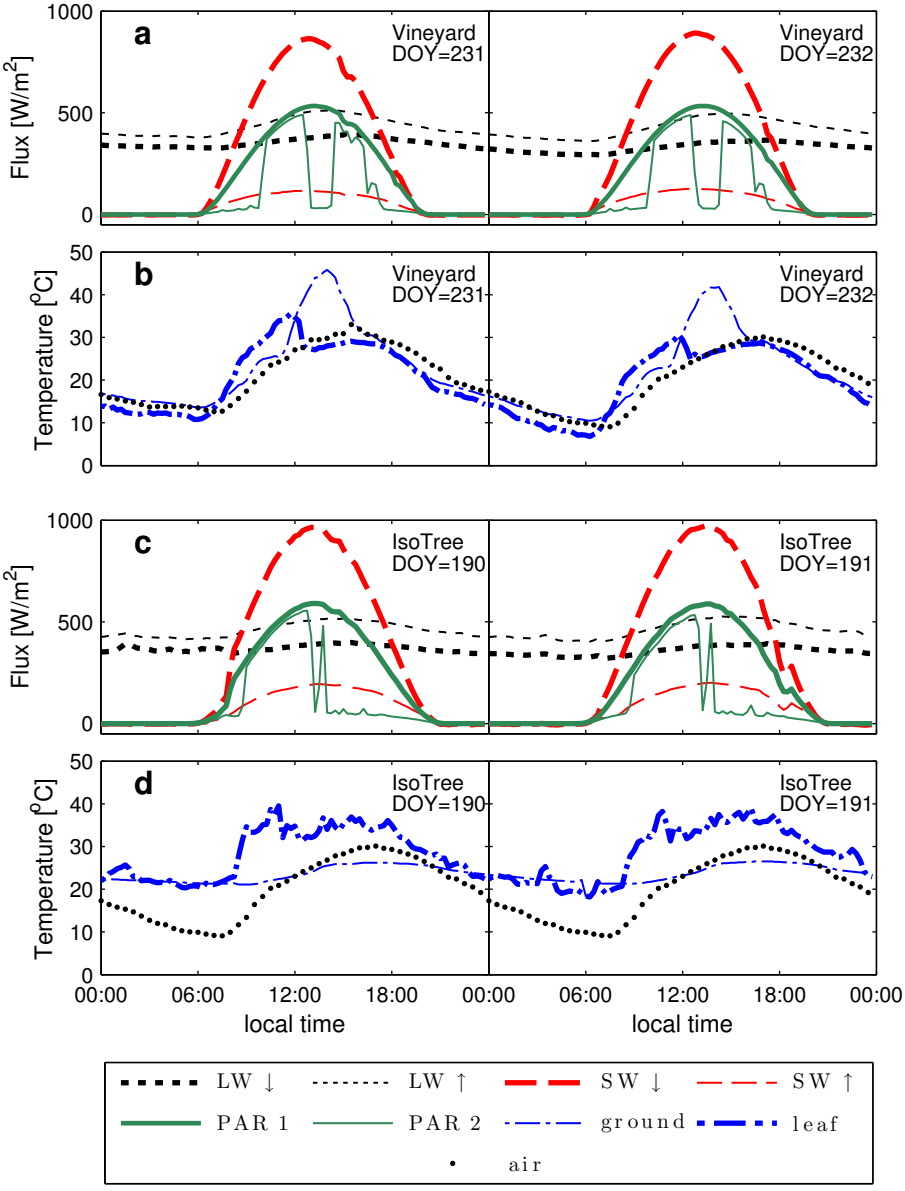

Figure 6: Measured values used to force the validation simulations for VINEYARD (a,b) and ISOTREE (c,d). Measurements include incoming longwave radiation from the sky (LW ↓), outgoing longwave radiation (LW ↑), incoming solar radiation (SW ↓), reflected/scattered solar radiation (SW ↑), incoming PAR radiation (PAR 1), PAR radiation after attenuation by vegetation (PAR 2), ground temperature, and leaf temperature. Air temperature is given only for reference as it is never used in any radiation calculations. Local time in (a,b) and (c,d) are PDT and MDT, respectively.

3.2.1. Radiative fluxes

Radiation was measured at several points within and around vegetation for three sets of wavelengths, as depicted by Fig. 7. Net radiation just above vegetation was measured using a CNR1 net radiometer (Campbell Scientific, Logan, UT, USA). The CNR1 measures incoming (downward) and reflected/scattered (upward) solar radiation using a pair of opposite-facing pyranometers, which can detect wavelengths in the range of 305-2800 nm. The CNR1 also measures incoming (downward) and reflected/emitted (upward) longwave radiation using a pair of opposite-facing pyrgeometers (5,000-50,0000 nm). The expected accuracy of the CNR1 for daily sums is ±10%.

For Vineyard, the CNR1 was mounted at the top of a 10-m tall tower. For IsoTree, the CNR1 was mounted on a steel pole that ran up the trunk of the tree and extended to a height just above the highest branches.

The attenuation of radiation through vegetation was measured using a pair of SQ-100 quantum (PAR) sensors (Apogee Instruments, Logan, UT, USA) which can measure wavelengths in the range of 410-660 nm. One upward-facing quantum sensor was co-located with the CNR1. Another quantum sensor was placed on a movable arm that could put the sensor within or below vegetation. For Vineyard, the lower quantum sensor was placed on the ground centered below a row of vegetation. The lower IsoTree quantum sensor was placed inside vegetation 1.8 m from the trunk, 85° clockwise from North, and 2.0 m from the ground. All radiation sensors were leveled using on-board bubble levels.

The model was driven by the measurements of the unobstructed upper-facing sensors mounted above vegetation. The incoming diffuse longwave flux was specified directly from the measurement of the upward-facing CNR1 pyrgeometer. The incoming PAR flux was specified using the reading of the quantum sensor. The incoming NIR flux was specified using the difference of the CNR1 pyrenometer and the quantum sensor readings. These two fluxes must then partitioned into the direct and diffuse components. We chose to use the process-based model REST-2 (Gueymard, 2008) instead of more traditional empirical models (e.g., Weiss and Norman, 1985; Spitters et al., 1986). We found that using the empirical models caused a substantial hysteresis in the diffuse fraction, which is likely due to the fact that their coefficients are site-specific. Several atmospheric parameters must be specified in the REST-2 model. Ozone and precipitable water amounts were calculated using the models of van Heuklon (1979) and Viswanadham (1981), respectively (Nitrogen scattering and absorption was neglected). Atmospheric turbidity was estimated for each of the experimental sites using the measurements of Flowers et al. (1969). Variation in the above mechanisms gave minimal changes to the diffuse fraction. Rather, Rayleigh scattering was the dominant mechanism, which is only a function of the measured atmospheric pressure.

3.2.2. Surface temperature

Leaf surface temperature, which is required to calculate radiative emission in the model, was measured for individual leaves using 40AWG chromel-constantan thermocouples (Omega Engineering, Stamford, CT, USA). Chromel-constantan

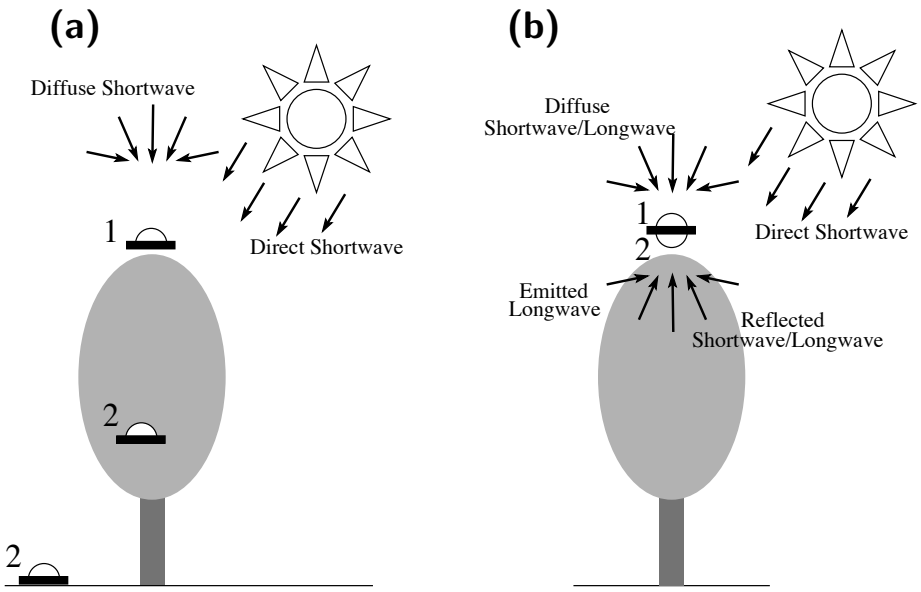

Figure 7: Schematic of radiation sensor placement with respect to vegetation intended to measure (a) attenuation of shortwave and (b) reflected/scattered irradiation. Sensors are labeled with numbers. (a) Each sensor in the figure consists of a co-located set of a pyrometer and quantum (PAR) sensor. Sensor pair **1** measures incoming unobstructed global shortwave irradiation, while sensor pair **2** measures incoming global shortwave irradiation after being attenuated by vegetation. (b) Sensor **1** consists of both a pyrometer and a pyrgeometer that measures incoming global shortwave and longwave irradiation, respectively. Sensor **2** consists of the same sensor set as **1**, except that they are downward facing.

was chosen over the traditional copper-constantan because of its lower thermal conductivity, which was reported by Tarnopolsky and Seginer (1999) to reduce conduction error. Thermocouples were attached to the center of the lower (abaxial) side of leaves. The insulated portion of the thermocouples were adhered to the leaf using Transpore™ medical tape (3M, St. Paul, MN, USA), which is permeable to air and moisture. To reduce contact resistance between the thermocouple and the leaf surface, a small amount of OMEGATHERM® thermally conductive paste (Omega Engineering, Stamford, CT, USA) was applied to the thermocouple tip. Measurements were simultaneously made on two leaves. For IsoTree, one was South-facing on the outside of the crown, and the other was North-facing in the inside the crown (both at heights of about 2 m). For Vineyard, one was at the top of the row, and the other was on the East face of the row at a height of about 1.5 m. The average of the two temperatures were used to specify T_L.

Ground surface temperature was measured at two locations near the radiation measurements using infrared thermometers: model SI-111 (Apogee Instruments, Logan, UT, USA) for Vineyard and model TN9 (ZyTemp, Hsin Chu, Taiwan) for IsoTree.

3.3. Validation results

In order to evaluate model performance, measured values from physical sensors were compared with values given by 'virtual sensors' placed in the simulated domain. The virtual sensors were placed at the locations of the downward-facing CNR1 sensors and the within-canopy PAR sensors (sensors labeled '**2**' in Fig. 7). Simulations were driven with upward-facing unobstructed measurements (sensors labeled '**1**' in Fig. 7).

Virtual sensors for reflected/scattered shortwave and longwave irradiation (downward-facing sensors) consisted of a control area that summed the energy (in Watts) of rays crossing through its face from either the bottom direction (downward-facing physical sensors) or the top direction (upward-facing physical sensors). The total incident energy was then divided by the virtual sensor's area to yield a flux value that could be compared against the sensor output. PAR attenuation virtual sensors (upward-facing) were similar, except that for the direct component (which is absent for a downward-facing sensor) they launched a single ray from the sun toward the sensor and calculated the fraction of energy that reached the sensor. They also summed contributions of diffuse PAR due to in-scattering.

Agreement between modeled and measured values was quantified by the root mean square error (RMSE) and the index of agreement (d) (Willmott, 1981). For traditional purposes, we also report the coefficient of determination (R^2) although it is commonly considered to be a flawed indicator of model performance.

For both Vineyard and IsoTree, the number of patches, volumes, and rays were chosen such that further increasing these values did not change results. The Vineyard case used 146×100 ground patches of size 0.5×0.5 m^2, with 512 rays

per volume (256 rays per patch). Each row of vegetation was discretized into 100×1×4 volumes (30 rows total). The IsoTree case used 100×100 ground patches of size 0.5×0.5 m^2, with 512 rays per volume (256 rays per patch). The tree crown was discretized into a uniform grid of 14×14×18 volumes. Volumes outside of an ellipsoid with principal radii of 2, 2, 3.25 m (x, y, z) were removed to form an approximately ellipsoidal-shaped crown.

3.3.1. Vineyard

Figure 8a shows the comparison for the downward-facing longwave sensor above the canopy for Vineyard. Results show good agreement throughout the diurnal cycle, with d and R^2 values of 99% and 98%, respectively. The greatest uncertainty in the simulation of longwave transport is the specification of surface temperatures. During periods of low solar radiation fluxes, surface temperatures are relatively constant throughout the canopy. Naturally, this is the period in which the model performs best, as a constant temperature distribution is assumed. During periods of intense solar fluxes, surface temperatures have high variability, and thus results contain more scatter. Adding a spatially-explicit model for leaf surface temperature would alleviate the issue of assuming a constant surface temperature. However, this is beyond the scope of this study, and will be addressed as part of future work.

A comparison of measured and simulated fluxes for the downward-facing shortwave sensor above the canopy shows good agreement throughout the day (Fig. 8b). The model under-predicts shortwave radiation for low sun angles. This could be due to various factors that are important for low sun angles, such as the model to predict the fraction of diffuse shortwave irradiation or terrain effects. We also found that increasing the leaf reflectivity improved results for low sun angles (not shown). It is possible that factors such as age (Schultz, 1996), chlorophyll content (Zarco-Tejada et al., 2005), and water content (Rodríguez-Pérez et al., 2007) could cause the leaves to be more reflective than the LOPEX samples. Regardless, model agreement is still very good with d and R^2 values of 98% (RMSE=10.3 W/m^2).

Figure 8c shows a comparison of measured and simulated values for the ratio of within-canopy to above-canopy fluxes of PAR, or attenuation through the canopy. The biggest difficulty for the model to predict attenuation is the inability to account for the effects of individual leaves. Due to leaf heterogeneity, there may be periods where sunflecks are able to easily penetrate the canopy and reach the sensor or other periods where an individual clump overly shades the sensor. As a result, outlier measurements occur. These data points can be seen in Fig. 6a, which are time periods when the attenuated PAR sensor reading has significant fluctuations that are not accompanied by fluctuations in the unobstructed sensor reading. The fact that these fluctuations are present in the data for multiple days suggests that they are geometry-related. Despite the presence of outlier points, the relatively high d value (95%) indicates that the model performs well on average.

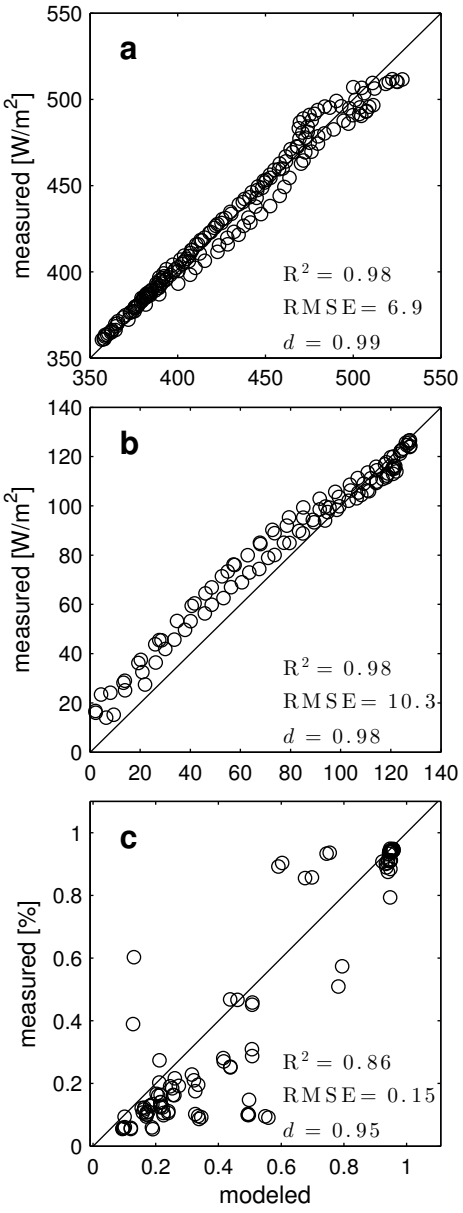

Figure 8: Comparison between measured and simulated values for the VINEYARD test case (a) reflected/emitted longwave radiation emanating from the canopy, (b) reflected shortwave radiation emanating from the canopy, and (c) fraction of PAR radiation transmitted through the canopy. Agreement is quantified by the coefficient of determination (R^2) and the correlation coefficient (r). Data points represent 15 min averaged values over two complete diurnal cycles.

3.3.2. IsoTree

Agreement between modeled and measured longwave fluxes for IsoTree (Fig. 9a) is very good for night, morning, and evening periods. This is a strong indication that the physical models are correct, and that total leaf area was specified with reasonable accuracy. We note that considering anisotropic emission was essential for correctly predicting longwave fluxes, as assuming isotropic emission resulted in a substantial flux under prediction. Longwave transport was more difficult to model during intense solar fluxes for IsoTree than Vineyard because of even larger variation in surface temperature. There were periods of the day when one or both leaf surface temperature measurements were shaded, and other periods when they were randomly shaded. This is shown in the data as dramatic fluctuations in temperature ($5-10°C$) over a relatively short time period (Fig. 6d). We consider this a limitation in the measurements and not the model. If mid-day data points are not considered, d increases to near 100%.

A noticeable hysteresis can be observed in the measured shortwave reflected/scattered data (Fig. 6c). The downward-facing measurement peaks several hours after the peak in the upward-facing measurement. This resulted in model over prediction before solar noon and under-prediction after noon. We hypothesized that this was due primarily to the four-story building directly to the East of the tree whose face consisted of light-colored brick and large windows. Although the building did not directly shade the tree for most of the day, it seemed plausible that the building was causing shading of shortwave irradiation on the adjacent ground in the morning and reflection in the late-day. To test this hypothesis, we placed a simulated building 30 m to the East of the tree. Reflection from the building was assumed to be Lambertian with an effective reflectivity for shortwave radiation of 0.7. Reflection of longwave radiation by the building was neglected. The goal was not to implement a highly realistic model for the presence of the building, but rather to test whether this could explain the hysteresis in the data. Inclusion of specular reflection and resolving the differences between the brick and windows would likely change the surface reflectivity value.

The addition of the simple building reflection model significantly reduced the hysteresis, and increased the R^2 value for shortwave reflection/scattering from 91% to 98% and d from 98% to 99%. This suggest that the tree model is performing as expected, and that much of the error is associated with the surroundings.

Modeling attenuation (Fig. 9c) was more difficult for IsoTree as it required an accurate specification of the highly three-dimensional tree shape and heterogeneous leaf distribution. The general trend of attenuation was in good agreement, indicating that the geometry and overall leaf area were accurately specified. Outlier points occurred, which were likely due to the influence of individual leaves/shoots. This can be clearly seen in the data (Fig. 6), where extreme fluctuations in the attenuated measurement occurred despite no accompanying fluctuations in the unobstructed sensor. Despite the outliers, the bulk of points were in good agreement with measurements (d=96%).

For the majority of the day, the presence of the building had no effect on

attenuation. However, in the early morning, the building directly shaded the lower sensor, causing a dramatic model over prediction. The building model increased the R^2 value for attenuation from 53% to 84% and d from 86% to 96%.

4. Model implementation

In addition to accurately modeling radiative transport in complex canopies, a primary goal of this study was to be able to apply the model over whole-canopy scales. This means the model must be very computationally efficient. This section presents serial and parallel implementation strategies that aim to allow for the simulation of very large computational domains using only a single consumer-level desktop workstation.

4.1. Serial implementation details

The serial implementation used the FORTRAN 90 standard. The primary strategy of the serial implementation was to exploit large available memory capacity and relatively low memory latency. This was done by pre-computing as much information as possible that could be stored in memory and re-used for multiple wavebands or time-of-day calculations. Quantities dependent on ray direction ($G(\theta')$, Γ, ρ'', f_V) were pre-computed for all possible incoming and outgoing ray direction combinations.

The greatest amount of efficiency was gained by pre-computing reflected and scattered ray trajectories. It is not necessary to actually calculate the trajectories of scattered rays, since rays were already launched and traced when diffuse exchange from patches was computed. Thus, if sufficient memory is available, the path traces that were performed for diffuse exchange can be stored in a pre-processing step and used as a 'table look-up' to efficiently compute scattering. The following must be stored for each patch/volume intersection along a ray's path in order to later calculate absorption and reflection/scattering:

1. **ID #:** A single-precision unsigned integer corresponding to a unique identifier for each patch/volume.

2. Δr**:** A single-precision real number that records the path length (Δr) of the ray through the volume. If the intersection was a patch, then $\Delta r = -1$.

This means that each ray intersection requires only 8 Bytes of memory storage. For the Vineyard case, this equated to roughly 50MB of data that needed to be stored.

The 'look-up' calculation of reflected energy leaving any given patch or volume only needs to be computed once. For example, imagine that 50 rays pass through a single volume, each of which will have some fraction of their energy scattered by that volume. The tracking of that scattered energy does not need to be computed 50 times, but rather one time. An initial pass of all ray traces are computed, and the amount of energy that needs to be reflected or scattered

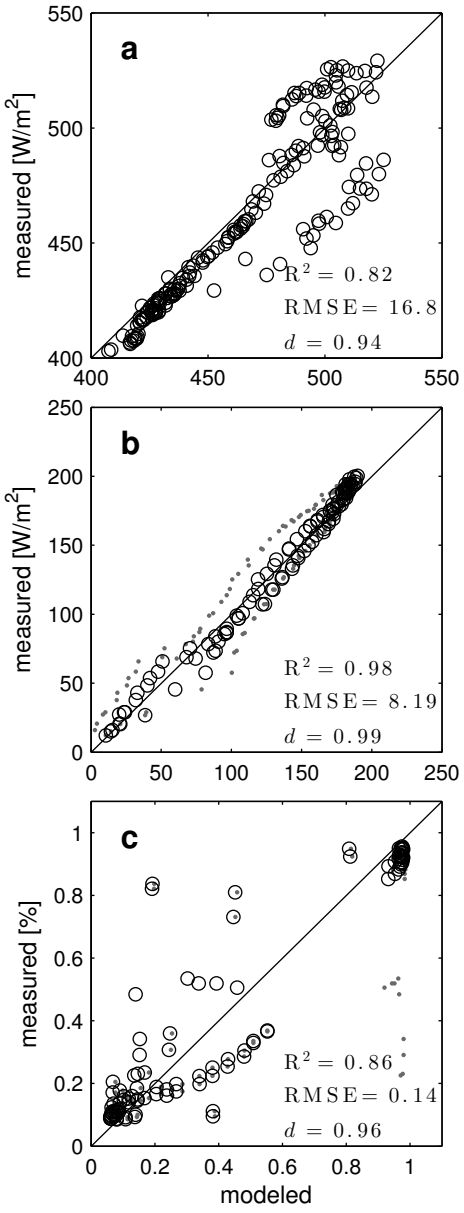

Figure 9: Comparison between measured and simulated values for the IsoTree test case (a) reflected/emitted longwave radiation emanating from the tree/ground, (b) reflected shortwave radiation emanating from the tree/ground, and (c) fraction of PAR radiation transmitted through the tree. Agreement is quantified by the coefficient of determination (R^2) and the correlation coefficient (r). Data points represent 15 min averaged values over two complete diurnal cycles. Circles and dots show results with and without the building model, respectively.

from each patch or volume is accumulated in a buffer. This buffer also has bins associated with incoming ray angle, since outgoing radiation will in general be a function of incoming angle. Subsequent passes are performed to recursively compute the reflected and scattered energy until the amount of remaining energy to be scattered becomes arbitrarily small.

For the two test cases, vegetation was comprised of a contiguous block of discrete cells. Areas of open space such as the space between vineyard rows were represented by a single volume and assigned an LAD value of zero, and thus computations were skipped. Similarly the ground consisted of a uniform grid of patches. This meant that patch and volume intersections were trivial, as intersections could be computed using only a few arithmetic operations and the 'floor' function. For arbitrary geometries, this approach may not be feasible in many cases. Therefore a hierarchical intersection algorithm would be necessary, which would likely lead to a significant decrease in performance.

4.2. Parallel implementation details

The parallel implementation is built for current GPUs and utilizes NVIDIA's OptiX (Parker et al., 2013) and CUDA development frameworks. We specifically leverage OptiX (a GPU ray tracing engine) to accelerate ray tracing within the simulation domain. The engine is supplied with kernels, which are individual functions designed to run on the GPU. These kernels define how rays are launched, how ray-object intersections are determined, and what happens in the event of a ray-object intersection. OptiX reassembles these kernels to run efficiently and in parallel on NVIDIA GPUs, and accelerates ray-object intersection tests. By doing so, it can take advantage of the large-scale parallelism and high throughput offered by modern GPUs. However, data must reside within the dedicated memory of the GPU. Relative to CPU memory, GPUs often have smaller amounts of resident memory, with current consumer and professional cards having around 1-6 GB of on-board GPU memory. The parallel implementation attempts to leverage highly optimized ray tracing in order to reduce the total amount of memory overhead, which allows the code to simulate very large domain sizes.

From a methodological standpoint, the parallel implementation differs in several ways from the serial implementation. First, OptiX ray launches are used to simultaneously generate the ray trajectories that transfer energy within the domain. Likewise, the intersection of these rays is also handled concurrently with OptiX using surface intersection routines. In essence, the GPU achieves high throughput on computations by having thousands of threads ready to execute on the GPU's multiprocessors. Second, rather than considering all possible $\mathbf{s}'$ directions for computing scattered energy, incoming directions were binned into a reduced number of discrete directions. This reduced memory requirements on the GPU by decreasing the amount of data that needed to be stored for each scattering iteration. Memory restrictions also meant that, unlike the serial implementation, pre-computing many quantities was not possible. Primarily, all ray trajectories were computed on the fly. This was helped by the fact that the underlying ray tracing operations are very efficient on the GPU

because OptiX is highly optimized for these computations. This also means that ray traces can be changed dynamically throughout the course of a simulation, which allows the geometry or number of ray launches to be varied. Additionally, the scattering phase functions and BRDFs were not pre-computed. The greatest expense in computing the scattering phase function in this fashion was calculating the diffuse component of the scattering phase function. We found that pre-computing the kernel function Ψ' (see Eq. B.2) on the CPU required relatively little memory, and gave a substantial overall increase in speed. It was also not possible to pre-calculate f_V, which was approximated by attenuating rays within the volume from which they were launched (see §2.4).

4.3. Computational performance

4.3.1. Execution time

The two validation simulations were used as benchmark cases to compare the serial and parallel implementations. The VINEYARD case used 12,000 vegetation volumes and 14,600 ground patches, with 512 rays per volume (256 rays per patch). The ISOTREE case used approximately 2,800 vegetation volumes and 10,000 ground patches, with 512 rays per volume (256 rays per patch). To ensure uniformity between the codes, scattering always proceeded for exactly 10 iterations (although much fewer is usually required). The total execution times including preprocessor calculations were normalized by the number of timesteps to get the average execution time per timestep. The cases were run using both parallel GPU C++ and serial FORTRAN versions of the code.

It is extremely important to point out that general comparisons between execution times for CPU and GPU codes are difficult and often misleading (Lee et al., 2010). Performance gains by the GPU are highly dependent on a wide array of factors, including the amount of optimization applied to either code and the specific GPU/CPU architectures. The quantitative comparison presented below is indented only to give a sense of the strengths and weaknesses of the two implementations, and not as an absolute measure of their merit.

The GPU version (NVIDIA GTX Titan card) averaged 28 and 7.0 seconds per timestep for VINEYARD and ISOTREE, respectively. The serial version (3.3 GHz Intel core) with gfortran's "-O3" optimization level ran the two cases in 598 and 120 seconds per timestep, respectively. That equates to an increase in speed by the GPU code of about 21x for VINEYARD and 17x ISOTREE. The ISOTREE case is not as strict of a test of code performance, since a relatively small fraction of rays intersect a patch or volume. This limits one of the greatest advantages of the GPU code, which is accelerated ray tracing. The VINEYARD case was a much stricter test, and highlights code performance. The CPU code had a strong advantage during the nighttime, as there was no ray tracing to perform. Longwave radiation at night could be calculated using pre-computed ray traces stored in memory. This resulted in comparable execution times for both implementations during the night. For every discrete calculation during the daytime, both codes had to perform ray tracing for direct shortwave exchange, which gave the GPU code a considerable advantage (>25x).

4.3.2. Scaling

Scaling of the parallel implementation was also performed in order to assess the code's ability to simulate very large domains. A virtual forest was created that consisted of a random distribution of tree crowns of varying size and shape, each with 5-500 cubical sub-volumes (Fig. 10). Scaling performance was evaluated by measuring the time to run domains with an increasing number of vegetation volumes and ground patches. The simulations used a constant number of rays per patch/volume. For shortwave and diffuse longwave calculations, each patch used 256 rays. Scattering/emission was performed for patches and volumes using 256 and 512 rays, respectively. To ensure uniformity, scattering always proceeded for exactly 10 iterations. The simulations were performed at solar noon, which is when computations are most intensive. Thus, execution times represent a 'worst case' scenario.

The scaling tests were performed on two different GPU cards. These included a relatively inexpensive commodity-level NVIDIA GeForce GTX 480 (released 2010), and a higher-end NVIDIA GTX Titan (released 2013). The GTX 480 has 480 CUDA Cores and 1.536 GBytes of memory, whereas the GTX Titan has 2688 CUDA Cores with 6.144 GBytes of memory. Execution time scaled nearly linearly with problem size on both cards (Fig. 11). As expected, the Titan consistently outperformed the GTX480. The speed-up obtained from the Titan was constant at a little over 2. Both cards were able to successfully execute the model up to a domain size of about 700K patches+volumes. The 700K domain completed execution in under 2,000 seconds on the Titan card. While domain sizes larger than this were able to be simulated, the performance of some larger domain sizes was inconsistent due to limits in the memory and computational organization capabilities of the current parallel implementation. Future work will focus on improving the computational performance of the parallel implementation and increasing these limits to simulate much larger domains.

This study demonstrates the feasibility using the model for very large problems with relatively standard hardware. It should be noted that the GPU implementation substantially outperforms the current serial implementation in terms of scaling. The serial code runs out of memory for problems much bigger than the VINEYARD test case. In order to run very large domains on the CPU, a scalable architecture (i.e., a supercomputer) is necessary. Otherwise, ray tracing and other quantities must be computed on the fly like in the GPU implementation. However, this would likely be too slow to be feasible.

5. Summary

A new model was developed and validated to simulate radiative transport in complex participating media with high computational efficiency. The model is based on ray tracing techniques, but uses deterministic scattering and reflection algorithms to increase efficiency. The model was applied to calculate the transport of both solar and terrestrial radiation in complex plant canopies.

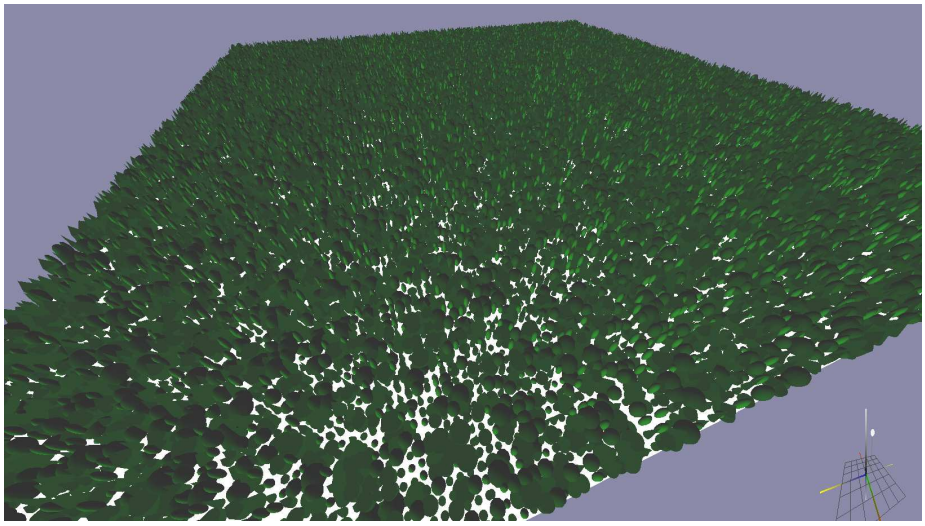

Figure 10: Screenshot of a test domain used in the scaling tests. This scene consists of approximately 440,000 volumes (30,000 trees) and 260,000 patches. Radiation calculations were performed at solar noon.

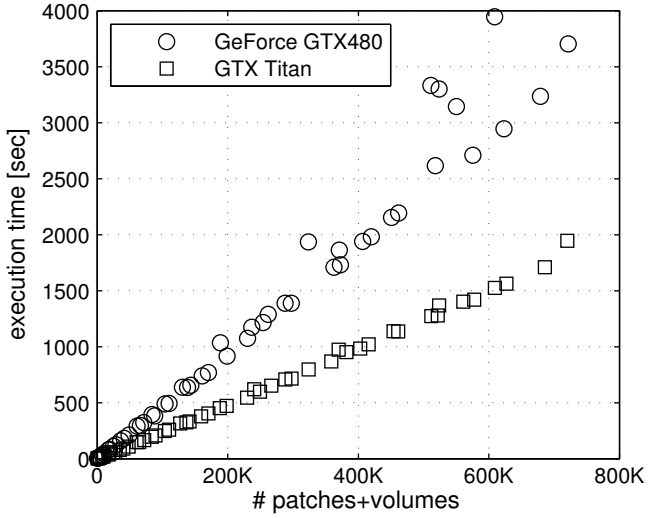

Figure 11: Execution time for the parallel implementation for a range of domain sizes. Tests were performed on two different GPU cards: NVIDIA GeForce GTX480, and NVIDIA GTX Titan.

Vegetation is resolved down to the sub-plant scale by discretizing individual plants into sub-volumes of leaves with constant physical properties. The model includes physics of radiative transfer commonly neglected in most models including anisotropic emission and scattering. The goal of the model was to be able to efficiently solve canopy-scale problems without the use of a supercomputer, and without compromising physical complexity.

The computational expense associated with including complex physics is afforded by performing computations on GPUs. The highly optimized NVIDIA OptiX framework was used to perform efficient ray tracing. This allowed the code to minimize memory requirements by leveraging efficient ray tracing. The model was tested up to problem sizes of about 700,000 patches+volumes, which demonstrated the feasibility of solving canopy-scale problems on a common desktop workstation.

The model was validated against field data collected in a grapevine canopy, and around a relatively isolated tree. Model predictions were compared against several sensors placed at various locations within the canopy that measured three separate wavelength bands. The validation experiment was designed such that model predictions of reflection, scattering, and emission by vegetation could be strictly evaluated in addition to the traditionally used through-canopy attenuation. The modeled and measured values were in good agreement, with model predictions generally well within the expected measurement error. The root mean square error of scattered shortwave flux predictions were around 10 W/m^2 (R^2, $d > 98\%$). Modeling of longwave emission was complicated by the inability to specify the 3D temperature distribution. Agreement was still very good, with index of agreement values of 99% and 94% for Vineyard and IsoTree, respectively. Through-canopy transmission measurements contained some scatter due to leaf-scale heterogeneity (i.e., 'clumping') that could not be accounted for in the model. Regardless, index of agreement values were still greater than 95%. Future work will involve further validation that includes more detailed representations of the radiative spectrum and leaf-scale heterogeneity through use of ground-based LiDAR systems. The model could also be adapted to remote sensing applications, which may include validation through a model intercomparison such as RAMI (Pinty et al., 2001).

Acknowledgments

The authors are indebted to J. Johnson and N. Miller, as well as numerous others for their support with the field experiments. This research was supported by National Science Foundation grants IDR CBET-PDM 113458, EPS 1208732, and AGS 1255662 and United States Department of Agriculture (USDA) project 5358-22000-039-00D. The use, trade, firm, or corporation names in this publication are for information and convenience of the reader. Such use does not constitute an endorsement or approval by the USDA or the Agricultural Research Service of any product or service to the exclusion of others that may be suitable. Any opinions, findings, and conclusions or recommendations expressed

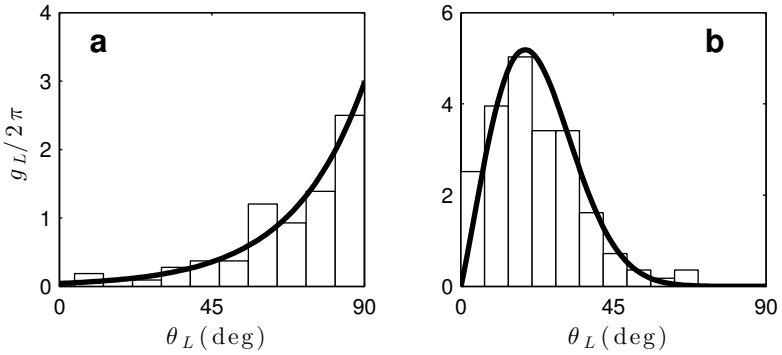

Figure A.12: Measured leaf angle distributions for (a) VINEYARD (Eq. A.2) and (b) ISOTREE (Eq. A.3). Bars show histograms of measured values. Solid lines show fitted PDF functions.

are those of the authors and do not necessarily reflect the views of the National Science Foundation.

Appendix A. Calculation of $G(\theta')$

To obtain the probability density function (PDF) of leaf orientation, the zenith angles θ_L of random leaves were measured using a digital protractor (leaves were assumed to be azimuthally symmetric). Note that in the following discussion we define leaf angle such that for a horizontal leaf $\theta_L = 0$ and for a vertical leaf $\theta_L = \pi/2$. By definition of g_L the following normalization relation must be satisfied (Ross, 1981)

$$\int_0^{\pi/2} g_L(\theta_L) \sin\theta_L \, d\theta_L \equiv 1. \tag{A.1}$$

The leaf angle measurements for VINEYARD appeared to follow an exponential probability distribution, whose PDF is given by

$$g_L(\theta_L; a) = Cae^{-a(\pi/2-\theta_L)}, \tag{A.2}$$

where a is the distribution parameter, which was found to be 2.7 for the PDF in Fig. A.12a, and C is a normalization factor that enforces Eq. A.1. ISOTREE measurements appeared to follow a Weibull distribution, whose PDF is given by

$$g_L(\theta_L; a, b) = C\frac{b}{a}\left(\frac{\theta_L}{a}\right)^{b-1} e^{-(\theta_L/a)^b}, \tag{A.3}$$

where a and b are the distribution shape and scale parameters, respectively. For ISOTREE $a = 2.1$ and $b = 0.45$ as shown by the PDF in Fig. A.12b.

The leaf probability density was then used to calculate $G(\theta')$ based on its definition as follows (Ross, 1981)

$$G(\theta') = \int_0^{\pi/2} g_L(\theta_L)\, \Psi \sin\theta_L \, d\theta_L, \tag{A.4}$$

where Ψ is a kernel function calculated according to (Shultis and Myneni, 1988)

$$\Psi = \begin{cases} |\mu\mu_L|, & |\cot\theta \cot\theta_L| > 1 \\ \\ \mu\mu_L \left(\dfrac{2}{\pi}\phi_t - 1\right) + \dfrac{2}{\pi}\sqrt{1-\mu^2}\sqrt{1-\mu_L^2}\sin\phi_t & \text{otherwise} \end{cases} \tag{A.5}$$

with

$$\mu = \cos\theta, \tag{A.6a}$$

$$\mu_L = \cos\theta_L, \quad \text{and} \tag{A.6b}$$

$$\phi_t = \cos^{-1}\left(-\cot\theta\cot\theta_L\right). \tag{A.6c}$$

This leads to G-functions for VINEYARD and ISOTREE, respectively, as

$$G(\theta') = Ca \int_0^{\pi/2} e^{-a(\pi/2-\theta_L)} \Psi \sin\theta_L \, d\theta_L, \tag{A.7a}$$

$$G(\theta') = C\frac{b}{a} \int_0^{\pi/2} \left(\frac{\theta_L}{a}\right)^{b-1} e^{-(\theta_L/a)^b} \Psi \sin\theta_L \, d\theta_L. \tag{A.7b}$$

Appendix B. Vegetation volume scattering phase function

Appendix B.1. Diffuse scattering phase function

Diffuse scattering from an individual leaf is assumed to be bi-Lambertian (Ross, 1981). The leaf scattering phase function is calculated as

$$\gamma_{L,D} = \begin{cases} \rho_{L,D}/\pi\,|\boldsymbol{s}\cdot\boldsymbol{s}_L| & (\boldsymbol{s}\cdot\boldsymbol{s}_L)(\boldsymbol{s}'\cdot\boldsymbol{s}_L) < 0 \\ \\ \tau_{L,D}/\pi\,|\boldsymbol{s}\cdot\boldsymbol{s}_L| & (\boldsymbol{s}\cdot\boldsymbol{s}_L)(\boldsymbol{s}'\cdot\boldsymbol{s}_L) > 0 \end{cases} \tag{B.1}$$

where $\rho_{L,D}$ and $\tau_{L,D}$ are the leaf reflectivity and transmissivity, respectively, and $\boldsymbol{s}\cdot\boldsymbol{s}_L$ is the projection of $\boldsymbol{s}$ onto $\boldsymbol{s}_L$ ($\boldsymbol{s}'\cdot\boldsymbol{s}_L$ is defined analogously).

The diffuse scattering phase function for a volume is calculated by integrating the leaf scattering phase function over all possible leaf angles

$$\Phi_D = \frac{1}{G(\theta')\,\omega_{L,D}} \int_0^{\pi/2} g_L\,\gamma_{L,D}\,\Psi' \sin\theta_L\,\mathrm{d}\theta_L, \tag{B.2}$$

where the kernel function Ψ' is evaluated as outlined by Myneni et al. (1988). The diffuse scattering phase function satisfies the normalization relation

$$\int_{4\pi} \left(\frac{\Phi_D}{4\pi}\right) \mathrm{d}\Omega \equiv 1. \tag{B.3}$$

Appendix B.2. Specular scattering phase function

The scattering phase function for specular reflection is calculated simply as the product of the Fresnel reflectance and the probability that there is a leaf normal correctly oriented for specular reflection (Vanderbilt and Grant, 1985; Knyazikhin and Marshak, 1991). This can be written as

$$\Phi_S = \frac{1}{G(\theta')\,\omega_{L,S}} \left[\frac{1}{2} g_L(\theta_L^{sp}) K \rho_{Fr}\right], \tag{B.4}$$

where

$$\cos\theta_L^{sp} = \frac{\cos\theta' + \cos\theta}{2\cos\theta_i}, \tag{B.5}$$

is the leaf normal direction for specular reflection from θ' to θ. The specular scattering phase function satisfies the normalization relation

$$\int_{4\pi} \left(\frac{\Phi_S}{4\pi}\right) \mathrm{d}\Omega \equiv 1. \tag{B.6}$$

References

Allen, W.A., Gausman, H.W., Richardson, A.J., Thomas, J.R., 1969. Interaction of isotropic light with a compact plant leaf. J. Opt. Soc. Am. 59, 1376–1379.

Asrar, G., Myneni, R.B., Choudhury, B.J., 1992. Spatial heterogeneity in vegetation canopies and remote sensing of absorbed photosynthetically active radiation: A modeling study. Remote Sens. Environ. 41, 85–103.

Ballaré, C.L., Scopel, A.L., Sánchez, R.A., 1990. Far-red radiation reflected from adjacent leaves: An early signal of competition in plant canopies. Science 247, 329–332.

Brakke, T.W., 1994. Specular and diffuse components of radiation scattered by leaves. Agric. For. Meteorol. 71, 283–295.

Buckley, T.N., Turnbull, T.L., Adams, M.A., 2012. Simple models for stomatal conductance derived from a process model: cross-validation against sap flux data. Plant Cell Environ. 35, 1647–1662.

Campbell, G.S., Norman, J.M., 1998. An Introduction to Environmental Biophysics. Second ed., Springer-Verlag, New York. 286 pp.

Cescatti, A., 1997. Modelling radiative transfer in discontinuous canopies of asymmetric crowns. I. Model structure and algorithms. Ecol. Model. 101, 263–274.

Chandrasekhar, S., 1950. Radiative Transfer. Dover Publications, New York. 416 pp.

Dauzat, J., Eroy, M.N., 1997. Simulating light regime and intercrop yields in coconut based farming systems. Eur. J. Agron. 7, 63–74.

Dimoudi, A., Nikolopoulou, M., 2003. Vegetation in the urban environment: mcroclimatic analysis and benefits. Energy and Buildings 35, 69–76.

Farmer, J.T., Howell, J.R., 1998. Comparison of Monte Carlo strategies for radiative transfer in participating media. Adv. Heat Transfer 31, 333–429.

Flowers, E.C., McCormick, R.A., Kurfis, K.R., 1969. Atmospheric turbidity over the United States, 1961-1966. J. Appl. Meteorol. 8, 955–962.

Ghosh, R., Sridhar, V.N., Venkatesh, H., Mehta, A.H., Patel, K.I., 1993. Linear polarization measurements of a wheat canopy. J. Remote Sensing 14, 2501–2508.

Gill, S.E., Handley, J.F., Ennos, A.R., Pauleit, S., 2007. Adapting cities for climate change: the role of the green infrastructure. Built Environ. 33, 115–133.

Govaerts, Y.M., 1995. A model of light scattering in three-dimensional plant canopies: A Monte Carlo ray tracing approach. Ph.D. thesis. Departement de Physique, Universitè Catholique de Louvain. Louvain Belgium.

Groot, A., 2004. A model to estimate light interception by tree crowns, applied to black spruce. Can. J. For. Res. 34, 788–799.

Gueymard, C.A., 2008. REST2: High-performance solar radiation model for cloudless-sky irradiance, illuminance, and photosynthetically active radiation - Validation with a benchmark dataset. Solar Energy 82, 272–285.

Harrison, A.W., Coombes, C.A., 1988. Angular distribution of clear sky short wavelength radiance. Solar Energy 40, 57–63.

Hay, R.K.M., Porter, J.R., 2006. The Physiology of Crop Yield. Second ed., Wiley-Blackwell, Hoboken, NJ. 330 pp.

Henderson, S.T., 1977. Daylight and Its Spectrum. Second ed., Wiley. 349 pp.

Horn, H.S., 1971. The Adaptive Geometry of Trees. Princeton University Press, Princeton, NJ. 146 pp.

Hosgood, G., Jacquemoud, S., Andreoli, G., Verdebout, J., Pedrini, A., Schmuck, G., 2005. Leaf Optical Properties EXperiment 93 (LOPEX93). Ispra, Italy.

Hottel, H.C., Cohen, E.S., 1958. Radiant heat exchange in a gas-filled enclosure: Allowance for nonuniformity of gas temperature. AlChE Journal 4, 3–14.

Hottel, H.C., Sarofim, A.R., 1967. Radiative Transfer. McGraw-Hill, New York. 520 pp.

Howell, J.R., Siegel, R., Mengüç, M.P., 2010. Thermal Radiation Heat Transfer. Fifth ed., CRC Press, Boca Raton, Florida. 987 pp.

Iwasa, Y., Cohen, D., Leon, J.A., 1985. Tree height and crown shape, as results of competitive games. J. Theoretical Biology 112, 279–297.

Jeans, J.H., 1917. The equations of radiative transfer of energy. Monthly Notices Royal Astronomical Society 78, 28–36.

Jonckheere, I., Fleck, S., Nackaerts, K., Muys, B., Copping, P., Weiss, M., Baret, F., 2004. Review of methods for in situ leaf area index determination Part I. Theories, sensors and hemispherical photography. Agric. For. Meteorol. 38, 33–44.

Jones, H.G., Vaughan, R.A., 2010. Remote Sensing of Vegetation: Principles, Techniques, and Applications. Oxford University Press, Oxford, UK. 400 pp.

Kimes, D.S., 1983. Dynamics of directional reflectance factor distributions for vegetation canopies. Appl. Opt. 22, 1364–1372.

Kimes, D.S., Kirchner, J.A., 1982. Radiative transfer model for heterogeneous 3-D scenes. Appl. Opt. 21, 4119–4129.

Knyazikhin, Y., Marshak, A., 1991. Fundamental equations of radiative transfer, in: Myneni, R.B., Ross, J. (Eds.), Photon-Vegetation Interactions: Applications in Remote Sensing and Plant Ecology. Springer-Verlag, pp. 9–43.

Kuusk, A., 1991. The hot spot effect in plant canopy reflectance, in: Myneni, R.B., Ross, J. (Eds.), Photon-Vegetation Interactions: Applications in Remote Sensing and Plant Ecology. Springer-Verlag, pp. 139–159.

Lee, V.W., Kim, C., Chhugani, J., Deisher, M., Kim, D., Nguyen, A.D., Satish, N., Smelyanskiy, M., Chennupaty, S., Hammarlund, P., Singhal, R., Dubey, P., 2010. Debunking the 100X GPU vs. CPU myth: An evaluation of throughput computing on the CPU and GPU, in: Proceedings of the 37th annual international symposium on computer architecture, Saint-Malo, France. pp. 451–460.

López-Lozano, R., Baret, F., García de Cortázar Atauri, I., Lebon, E., Tisseyre, B., 2011. 2D approximation of realistic 3D vineyard row canopy representation for light interception (fIPAR) and light intensity distribution on leaves (LIDIL). Eur. J. Agron. 35, 171–183.

Miller, N.E., Stoll, R., Mahaffee, W., Neill, T.M., Pardyjak, E., 2014. An experimental study of momentum and heavy particle transport in a trellised agricultural canopy. Submitted for review to Agric. For. Meteorol.

Modest, M.F., 2013. Radiative Heat Transfer. Third ed., Academic Press. 904 pp.

Monteith, J.L., Unsworth, M.H., 2008. Principles of environmental physics. third ed., Academic Press, UK.

Murray, R.C., 2011. Tree Biology Notebook: An Introduction to the Science and Ecology of Trees. Revised ed., STL Publishing. 266 pp.

Myneni, R.B., Gutschick, V.P., Asrar, G., Kanemasu, E.T., 1988. Photon transport in vegetation canopies with anisotropic scattering Part I. scattering phase functions in one angle. Agric. For. Meteorol. 42, 1–16.

Nilson, T., Kuusk, A., 1989. A reflectance model for the homogeneous plant canopy and its inversion. Remote Sens. Environ. 27, 157–167.

Nogués, S., Allen, D.J., Morison, J.I.L., Baker, N.R., 1998. Ultraviolet-B radiation effects on water relations, leaf development, and photosynthesis in droughted pea plants. Plant Physiology 117, 173–181.

Norman, J.M., Welles, J.M., 1983. Radiative transfer in an array of canopies. Agron. J. 75, 481–488.

North, P.R.J., 1996. Three-dimensional forest light interaction model using a Monte Carlo method. IEEE Trans. Geosci. Remote Sens. 34, 946–956.

Owens, J.D., Luebke, D., Govindaraju, N., Harris, M., Krüger, J., Lefohn, A.E., Purcell, T.J., 2007. A survey of general-purpose computation on graphics hardware. Computer Graphics Forum 26, 80–113.

Parker, S.G., Friedrich, H., Luebke, D., Morley, K., Bigler, J., Hoberock, J., McAllister, D., Robison, A., Dietrich, A., Humphreys, G., McGuire, M., Stich, M., 2013. GPU ray tracing. Commun. ACM 56, 93–101.

Passioura, J.B., 1973. Sense and nonsense in crop simulation. J. Aust. I. Agr. Sci. 39, 181–183.

Pinty, B., Gobron, N., Widlowski, J.L., Gerstl, S.A.W., Verstraete, M.M., Antunes, M., Bacour, C., Gascon, F., Gastellu, J.P., Goel, N., Jacquemoud, S., North, P., Quin, W., Thompson, R., 2001. Radiation transfer model intercomparison (rami) exercise. J. Geophys. Research 106, 11,937–11,956.

Reyna, E., Badhwar, G.D., 1985. Inclusion of specular reflectance in vegetative canopy models. IEEE Trans. Geosci. Remote Sens. 23, 731–736.

Rodríguez-Pérez, J.R., no, D.R., Carlisle, E., Ustin, S., Smart, D.R., 2007. Evaluation of hyperspectral reflectance indexes to detect grapevine water status in vineyards. Am. J. Enol. Vitic. 58, 302–317.

Ross, J., 1981. The Radiation Regime and Architecture of Plant Stands. Dr. W. Junk Publishers, The Hague, The Netherlands. 424 pp.

Roujean, J.L., Leroy, M., Deschamps, P.Y., 1992. A bidirectional reflectance model of the earth's surface for the correction remote sensing data. J. Geophys. Research 97, 455–468.

Russell, G., Jarvis, P.G., Monteith, J.L., 1989. Absorption of radiation by canopies and stand growth, in: Russell, G., Marshall, B., Jarvis, P.G. (Eds.), Plant Canopies: Their Growth, Form and Function. Cambridge University Press, Cambridge, UK, pp. 21–40.

Saff, E.B., Kuijlaars, A.B.J., 1997. Distributing many points on a sphere. Math Intell. 19, 5–11.

Schultz, H.R., 1996. Leaf absorptance of visible radiation in *vitis vinifera l.*: estimates of age and shade effects with a simple field method. Scientia Horticulturae 66, 93–102.

Shultis, J.K., Myneni, R.B., 1988. Radiation transfer in vegetation canopies with anisotropic scattering. J. Quant. Spectrosc. Radiat. Transfer 39, 115–129.

Sinoquet, H., Le Roux, X., Adam, B., Ameglio, T., Daudet, F.A., 2001. RATP: a model for simulating the spatial distribution of radiation absorption, transpiration and photosynthesis within canopies: application to an isolated tree crown. Plant Cell Environ. 24, 395–406.

Soler, C., Sillion, F.X., Blaise, F., Dereffye, P., 2003. An efficient instantiation algorithm for simulating radiant energy transfer in plant models. ACM Transactions on Graphics 22, 204–233.

Spitters, C.J.T., Toussaint, H.A.J.M., Goudriaan, J., 1986. Separating the diffuse and direct component of global radiation and its implications for modeling canopy photosynthesis: Part I. components of incoming radiation. afm 38, 217–229.

Stadt, K.J., Lieffers, V.J., 2000. MIXLIGHT: a flexible light transmission model for mixed-species forest stands. Agric. For. Meteorol. 102, 235–252.

Tarnopolsky, M., Seginer, I., 1999. Leaf temperature error from heat conduction along thermocouple wires. Agric. For. Meteorol. 93, 185–194.

van Heuklon, T.K., 1979. Estimating atmospheric ozone for solar radiation models. Solar Energy 22, 63–68.

Vanderbilt, V.C., Grant, L., 1985. Plant canopy specular reflectance model. IEEE Trans. Geosci. Remote Sens. 23, 722–730.

Viswanadham, Y., 1981. The relationship between total precipitable water and surface dew point. J. Appl. Meteorol. 20, 3–8.

Wang, Y.P., Jarvis, P.G., 1990. Description and validation of an array model - MAESTRO. Agric. For. Meteorol. 51, 257–280.

Weiss, A., Norman, J.M., 1985. Partitioning solar radiation into direct and diffuse, visible and near-infrared components. Agric. For. Meteorol. 34, 205–213.

Willmott, C.J., 1981. On the validation of models. Phys. Geogr. 2, 184–194.

Zarco-Tejada, P.J., Berjón, A., López-Lozano, R., Miller, J.R., Martín, P., Cachorro, V., González, M.R., de Frutos, A., 2005. Assessing vineyard condition with hyperspectral indices: Leaf and canopy reflectance simulation in a row-structured discontinuous canopy. Remote Sens. Env. 99.